Static force from generalized Wilson loops on the lattice using the gradient flow

Nora Brambilla,[1,2,3,*] Viljami Leino,[4,5,†] Julian Mayer-Steudte,[1,3,‡] and Antonio Vairo[1,§]

[1]*Technical University of Munich, TUM School of Natural Sciences, Physics Department, James-Franck-Strasse 1, 85748 Garching, Germany*

[2]*Institute for Advanced Study, Technical University of Munich, Lichtenbergstrasse 2a, 85748 Garching, Germany*

[3]*Munich Data Science Institute, Technical University of Munich, Walther-von-Dyck-Strasse 10, 85748 Garching, Germany*

[4]*Helmholtz Institut Mainz, Staudingerweg 18, 55128 Mainz, Germany*

[5]*Institut für Kernphysik, Johannes Gutenberg-Universität Mainz, Johann-Joachim-Becher-Weg 48, 55128 Mainz, Germany*

(Received 26 January 2024; accepted 23 May 2024; published 21 June 2024)

The static QCD force from the lattice can be used to extract $\Lambda_{\overline{\mathrm{MS}}}$, which determines the running of the strong coupling. Usually, this is done with a numerical derivative of the static potential. However, this introduces additional systematic uncertainties; thus, we use another observable to measure the static force directly. This observable consists of a Wilson loop with a chromoelectric field insertion. We work in the pure SU(3) gauge theory. We use gradient flow to improve the signal-to-noise ratio and to address the field insertion. We extract $\Lambda_{\overline{\mathrm{MS}}}^{n_f=0}$ from the data by exploring different methods to perform the zero-flow-time limit. We obtain the value $\sqrt{8t_0}\Lambda_{\overline{\mathrm{MS}}}^{n_f=0} = 0.629^{+22}_{-26}$, where t_0 is a flow-time reference scale. We also obtain precise determinations of several scales: r_0/r_1, $\sqrt{8t_0}/r_0$, $\sqrt{8t_0}/r_1$, and we compare these to the literature. The gradient flow appears to be a promising method for calculations of Wilson loops with chromoelectric and chromomagnetic insertions in quenched and unquenched configurations.

DOI: 10.1103/PhysRevD.109.114517

I. INTRODUCTION

The Standard Model of particle physics is one of the most precisely tested theories. A precise knowledge of the Standard Model parameters is a necessary condition to work out accurate perturbative predictions, and to compare them with high-precision experimental measurements. Quantum chromodynamics (QCD) is the sector of the Standard Model that describes the strong interaction. It is a field theory based on the gauge group SU(3) that depends on just one coupling, g, or equivalently $\alpha_s = g^2/(4\pi)$. The coupling may be traded at any time with an intrinsic scale; in the $\overline{\mathrm{MS}}$ scheme, this is $\Lambda_{\overline{\mathrm{MS}}}$. Once renormalized, α_s is small at energy scales much larger than $\Lambda_{\overline{\mathrm{MS}}}$, a property known as asymptotic freedom, but it becomes of order 1 at energy scales close to $\Lambda_{\overline{\mathrm{MS}}}$. At high energies, we can rely on weak coupling perturbation theory to compute QCD observables.

The value of $\Lambda_{\overline{\mathrm{MS}}}$, or equivalently α_s, at a large energy scale can be determined by comparing some high-energy observable computed in weak coupling perturbation theory with data. A viable alternative is to replace data with lattice QCD computations—i.e., the exact evaluation of the observable in QCD via Monte Carlo computations. For the current status of $\Lambda_{\overline{\mathrm{MS}}}$ extractions from lattice QCD, see for example the recent reviews [1,2]. While in the last several years, lattice extractions of $\Lambda_{\overline{\mathrm{MS}}}$ have been mostly done in QCD with dynamical quarks, the interest towards the running of the coupling in the pure gauge version of QCD—i.e., without dynamical quarks, also called quenched QCD—has been recently reignited [3]. With modern lattice methods, the extraction of the coupling from the pure gauge theory can be done much more precisely nowadays than in the past, when quenched calculations were the only viable option.

The static energy is a well-understood quantity in lattice QCD [4,5] that can be used to set the lattice scale [6]. Furthermore, the static energy is an observable that can be used to extract $\Lambda_{\overline{\mathrm{MS}}}$ by comparing its perturbative

*nora.brambilla@tum.de
†viljami.leino@uni-mainz.de
‡julian.mayer-steudte@tum.de
§antonio.vairo@tum.de

expression with lattice data at short distances. The QCD scale $\Lambda_{\overline{\rm MS}}$ has been extracted from the static energy both in pure gauge [7–11] and with dynamical fermions [12–18].

In lattice QCD, the static energy suffers from a linear divergence and needs to be renormalized. In dimensionally regularized perturbation theory, this divergence becomes a renormalon of mass dimension 1. For these reasons, it presents some advantages to look at the derivative of the static energy, which is the static force. The static force is not affected by linear divergences in lattice QCD or by renormalons of mass dimension 1 in dimensional regularization, yet it contains all the relevant information on the running of the strong coupling, as this is entirely encoded in the slope of the static energy. The force is known up to next-to-next-to-next-to-leading logarithmic accuracy in the coupling [19–24].

The derivative of the static energy performed numerically on lattice data introduces additional systematic uncertainties. Therefore, it may be advantageous to compute the force directly from a suitable observable [25–27]. This observable consists of a Wilson loop with a chromoelectric field insertion. A difficulty related to this observable is that field insertions on Wilson loops when evaluated on the lattice have a bad signal-to-noise ratio and a slow convergence to the continuum limit originating from the discretization of the field components. This was studied in a previous work [28]. In this work, to overcome the difficulty, we rely on the gradient flow method [29–31] to improve the signal-to-noise ratio and to remove the discretization effects of the field components. Wilson loops smeared with gradient flow have been studied before in terms of Creutz ratios [32–34]. In Ref. [35], the Wilson line correlator in the Coulomb gauge was measured at finite T with gradient flow. To our knowledge, this was the first time the gradient flow was applied to the force directly. Furthermore, this study also serves as a preparation for the study of similar Wilson loops with field insertions appearing in the computation of several observables in the context of nonrelativistic effective field theories. New methods for integrating the gradient flow equations, based on Runge-Kutta methods, have been developed and implemented during the last few years [36]. The force in gradient flow, besides that with lattice QCD, can also be computed analytically in perturbation theory. In perturbation theory, the static force at finite flow time is known at one-loop order [37].

The paper is structured as follows: In Sec. II, we discuss the theoretical background: we introduce the gradient flow and the static force at zero and finite flow time, in continuum and on the lattice. The lattice setup is described in Sec. III, and in Sec. IV we show our numerical results and perform the continuum limits. Finally, in Sec. V, we discuss our results and extract $\Lambda_{\overline{\rm MS}}^{n_f=0}$. Preliminary results based on these data have appeared before in conference proceedings [38,39].

II. THEORETICAL BACKGROUND

A. The static force

The static energy $V(r)$ in Euclidean QCD is related to a rectangular Wilson loop $W_{r\times T}$ with temporal extent from 0 to T and spatial extent r [40] by

$$V(r)=-\lim_{T\to\infty}\frac{\ln\langle{\rm Tr}(PW_{r\times T})\rangle}{T}=-\frac{1}{a}\lim_{T\to\infty}\frac{\langle{\rm Tr}(PW_{r\times(T+a)})\rangle}{\langle{\rm Tr}(PW_{r\times T})\rangle}, \tag{1}$$

$$W_{r\times T}=\left\{\exp\left(i\oint_{r\times T}dz_\mu gA_\mu\right)\right\}, \tag{2}$$

where a is the lattice spacing, g the strong coupling, Tr the trace over the color matrices, and P is the path-ordering operator for the color matrices. In dimensional regularization, the static energy has a renormalon ambiguity of order $\Lambda_{\rm QCD}$, while on the lattice there is a linear divergence of order $1/a$ coming from the self-energy of the Wilson line. Both the perturbative and lattice problems manifest as a constant shift to the potential. This may be renormalized by fixing the potential to a given value at a given point r^*:

$$V^r(r)=V(r)-V(r^*). \tag{3}$$

Alternatively, taking the derivative removes the divergent constant, and we obtain a renormalized quantity, the static force.

The static force $F(r)$ is defined as the derivative of the static energy:

$$F_{\partial V}(r)=\partial_r V(r). \tag{4}$$

In perturbation theory, the static force is known up to next-to-next-to-next-to-leading logarithmic order ($\rm N^3LL$) [19–24]. On the lattice, this derivative is evaluated from the static energy data either with interpolations or with finite differences, which leads to increased systematic errors. It is possible, however, to carry out the derivative of the Wilson lines at the level of Eq. (2), and rewrite the force as [25–27]

$$F_E(r)=-\lim_{T\to\infty}\frac{i}{\langle{\rm Tr}(PW_{r\times T}\rangle}\times\left\langle{\rm Tr}\left(P\left\{\exp\left(i\oint_{r\times T}dz_\mu gA_\mu\right)\hat{\mathbf{r}}\cdot g\mathbf{E}(\mathbf{r},t^*)\right\}\right)\right\rangle \tag{5}$$

$$=-\lim_{T\to\infty}i\frac{\langle{\rm Tr}\{PW_{r\times T}\hat{\mathbf{r}}\cdot g\mathbf{E}(\mathbf{r},t^*)\}\rangle}{\langle{\rm Tr}(PW_{r\times T}\rangle}, \tag{6}$$

where the expression in the numerator consists of a static Wilson loop with a chromoelectric field insertion on the temporal Wilson line at position t^*, and $\hat{\mathbf{r}}$ is the spatial

direction of the quark-antiquark pair separation; t^* can be chosen arbitrarily. Since both expressions for the force represent the same renormalized quantity, it holds in the continuum that $F_E = F_{\partial V} = F$.

B. Gradient flow

We rely on the gradient flow method [29–31] for measuring Wilson loops with and without chromoelectric field insertions. The gradient flow is a continuous transformation of the gauge fields toward the minimum of the Yang-Mills gauge action along a fictitious flow time τ_F:

$$\dot{B}_\mu(\tau_F, x) = D_\nu G_{\nu\mu} = -g_0^2 \frac{\delta S_{\mathrm{YM}}[B]}{\delta B_\mu(\tau_F, x)}, \tag{7}$$

$$B_{\mu|\tau_F=0} = A_\mu, \tag{8}$$

$$G_{\mu\nu} = \partial_\mu B_\nu - \partial_\nu B_\mu + [B_\mu, B_\nu], \quad D_\mu = \partial_\mu + [B_\mu, .], \tag{9}$$

where $B_\mu(\tau_F)$ are the flowed gauge fields at flow time τ_F, with the SU(3) QCD gauge fields A_μ as the initial condition at zero flow time; S_{YM} is the Yang-Mills action evaluated with the flowed gauge fields; $G_{\mu\nu}$ is the field strength tensor evaluated with the flowed gauge fields; and D_μ is the gauge covariant derivative. The flow depends on the local neighboring gauge field values through the derivative of the action with respect to the gauge field at position x, and its characteristic range is given by the flow radius $\sqrt{8\tau_F}$. This results in a smearing that cools off systematically the ultraviolet physics and automatically renormalizes gauge-invariant observables [41,42]. Furthermore, we introduce the reference scale t_0 [31], defined implicitly through the expectation value of the action density

$$E = \frac{1}{4} G^a_{\mu\nu} G^a_{\mu\nu}, \tag{10}$$

as

$$\tau_F^2 \langle E \rangle|_{\tau_F = t_0} = 0.3. \tag{11}$$

The gradient flow equation is adapted for flowed link variables $V_{\tau_F}(\mu, x)$ on the lattice as

$$\begin{aligned} \dot{V}_{\tau_F}(x,\mu) &= -g_0^2 \big(\partial_{x,\mu} S_{\mathrm{Gauge}}(V_{\tau_F})\big) V_{\tau_F}(x,\mu), \\ V_{\tau_F}(x,\mu)|_{\tau_F=0} &= U_\mu(x), \end{aligned} \tag{12}$$

where $S_{\mathrm{Gauge}}(V_{\tau_F})$ is some lattice gauge action evaluated with the flowed link variables, $\partial_{x,\mu}$ is the derivative with respect to $V_{\tau_F}(x,\mu)$, and $U_\mu(x)$ is the original SU(3) link variable. The flowed link variables of a gauge field configuration depend uniquely on the initial gauge field configuration U—i.e., $V_{\tau_F} = V_{\tau_F}(U)$—and flowed observables are obtained by replacing the original link variables with the flowed link variables: $O(\tau_F) = O|_{U=V_{\tau_F}}$. The flowed expectation value of O is evaluated on the flowed gauge ensemble and can be written as

$$\langle O(\tau_F) \rangle = \frac{1}{Z} \int \mathcal{D}[U] e^{-S_E[U]} O[V_{\tau_F}(U)], \tag{13}$$

which is still a path integral with the Euclidean action S_E of the original zero-flow-time theory. Therefore, on the lattice, the expectation value is given by

$$\langle O(\tau_F) \rangle \approx \frac{1}{N} \sum_{U, p(U) \propto e^{-S_E}} O(V_{\tau_F}(U)), \tag{14}$$

where N is the number of gauge fields. We solve the gradient flow on the lattice by an iterative Runge-Kutta implementation for the SU(3) matrices. We use either a fixed step-size algorithm [31] or an adaptive step-size algorithm [36,43].

C. The perturbative static force at finite flow time

The one-loop formula for the static force in gradient flow is [37]

$$\begin{aligned} F(r,\tau_F) = \frac{\alpha_S(\mu) C_F}{r^2} \Bigg[& \left(1 + \frac{\alpha_S}{4\pi} a_1\right) \mathcal{F}_0(r,\tau_F) \\ & + \frac{\alpha_S}{4\pi} \beta_0 \mathcal{F}^L_{\mathrm{NLO}}(r,\tau_F,\mu) + \frac{\alpha_S C_A}{4\pi} \mathcal{F}^F_{\mathrm{NLO}}(r,\tau_F) \Bigg] \\ & + \mathcal{O}(\alpha_S^3), \end{aligned} \tag{15}$$

with $C_F = (N_C^2 - 1)/(2N_C)$, $C_A = N_C$, $N_C = 3$ the number of colors, $\beta_0 = 11C_A/3 - 2n_f/3$, n_f the number of flavors, and $a_1 = 31C_A/9 - 10n_f/9$. The functions $\mathcal{F}_0(r,\tau_F)$ and $\mathcal{F}^L_{\mathrm{NLO}}(r,\tau_F,\mu)$ are given analytically with

$$\mathcal{F}_0(r,\tau_F) = \mathrm{erf}\left(\frac{r}{\sqrt{8\tau_F}}\right) - \frac{r}{\sqrt{2\pi\tau_F}} \exp\left(-\frac{r^2}{8\tau_F}\right), \tag{16}$$

$$\begin{aligned} \mathcal{F}^L_{\mathrm{NLO}}(r,\tau_F,\mu) = & \log(\mu^2 r^2) \mathcal{F}_0(r,\tau_F) \\ & + \log\left(\frac{8\tau_F}{r^2} e^{\gamma_{\mathrm{E}}}\right) \mathcal{F}_0(r,\tau_F) \\ & - \frac{r}{\sqrt{2\pi\tau_F}} \Bigg[e^{-\frac{r^2}{8\tau_F}} M^{(1,0,0)}\left(0, \frac{1}{2}, \frac{r^2}{8\tau_F}\right) \\ & + M^{(1,0,0)}\left(\frac{1}{2}, \frac{3}{2}, -\frac{r^2}{8\tau_F}\right) \Bigg], \end{aligned} \tag{17}$$

where γ_{E} is the Euler-Mascheroni constant and $M(a,b,z)$ is the confluent hypergeometric function, defined by

TABLE I. Numerical values of the coefficients c_n appearing in Eq. (20).

c_1	−0.0501648
c_2	0.526758
c_3	−5.55177
c_4	45.8753
c_5	−147.8
c_6	463.906
c_7	−851.741
c_8	884.315
c_9	−499.105
c_{10}	121.773

$$M(a,b,z)=\sum_{k=0}^{\infty}\frac{(a)_k}{(b)_k}\frac{z^k}{k!} \tag{18}$$

with $(x)_k=\Gamma(x+k)/\Gamma(x)$, and

$$M^{(1,0,0)}(a,b,z)=\frac{\partial}{\partial a}M(a,b,z). \tag{19}$$

For $r>\sqrt{\tau_F}$, we approximate $\mathcal{F}^F_{\rm NLO}$ with the polynomial

$$\mathcal{F}^F_{\rm NLO}(\xi=r/\sqrt{\tau_F})=\sum_{n=1}^{10}\frac{c_n}{n!}\left(\frac{\xi}{1+\xi/C_a}\right)^n e^{-\xi}+\frac{44-C_b}{C_a+\xi^2}+\frac{C_b\xi^2}{\xi^4+C_c}, \tag{20}$$

where $C_a=109.358$, $C_b=43.8438$, $C_c=404.790$, and c_n values are listed in Table I. In practice, the computation of $M^{(1,0,0)}$ takes a considerable amount of time, which is a problem for fitting this function. Those terms depend only on the flow-time ratio τ_F/r^2; hence, we precompute them on a fine flow-time ratio grid, and we use spline interpolations for further calls of the perturbative formula.

The one-loop formula has an explicit dependence on the renormalization scale μ in the form of $\log(\mu^2r^2)$ and an implicit dependence through the perturbative strong coupling $\alpha_s(\mu)$. At zero flow time, the only scale is the distance r; therefore, setting $\mu=1/r$ is a natural choice. At large flow time, r is negligible with respect to $\sqrt{8\tau_F}$, and therefore, the natural choice is $\mu=1/\sqrt{8\tau_F}$. A parametrization of μ that interpolates between these two limiting cases is $\mu=1/\sqrt{r^2+8\tau_F}$ [37]. Because in our lattice calculations we are not collecting data at large flow time, we adopt in this work the more general parametrization

$$\mu(r,\tau_F)=\frac{1}{\sqrt{sr^2+8b\tau_F}}. \tag{21}$$

At zero flow time, $\mu(r,0)=1/(\sqrt{s}r)$, and we can interpret $\sqrt{s}$ as a scale-variation parameter with central value 1. At intermediate-flow-time values—i.e., $\sqrt{8\tau_F}$ of the order of r—the parameter b defines an effective flowed distance. Starting from three loops, an ultrasoft (us) scale of order α_s/r also enters the static force equations at zero flow time [19]. For the scope of this paper, we set the ultrasoft scale to be $\mu_{\rm us}=C_A\alpha_s(1/r)/(2r)$.

We renormalize the coupling in the $\overline{\rm MS}$ scheme; hence, both α_s and the scale $\Lambda_{\overline{\rm MS}}$ are defined in that scheme. The scale $\Lambda_{\overline{\rm MS}}$ can be obtained by comparing the perturbative expression of the force with lattice data. Since we work in the pure SU(3) theory, the comparison provides $\Lambda_0\equiv\Lambda_{\overline{\rm MS}}^{n_f=0}$.

The small-flow-time expansion of r^2F reads

$$r^2F(r,\tau_F)\approx r^2F(r,\tau_F=0)+\frac{\alpha_s^2C_F}{4\pi}[-12\beta_0-6C_Ac_L]\frac{\tau_F}{r^2}, \tag{22}$$

with $c_L=-22/3$. We remark that $[-12\beta_0-6C_Ac_L]=8n_f$, which is 0 in this study ($n_f=0$). This means that at small flow time, the static force approaches a constant behavior, and that corrections to it are smaller than $\alpha_s^2\tau_F/r^2$; $r^2F(r,\tau_F=0)$ is r^2 times the one-loop perturbative force at zero flow time.

The static force at zero flow time is known up to N^{3}LL accuracy [19–24], and the higher loop contributions are crucial for the extraction of the Λ_0 parameter. To benefit from this knowledge, we model the flowed force with the one-loop expression at finite flow time, and we demand it to converge to the expression at arbitrary order at zero flow time. In terms of equations, our model function is given by

$$r^2F(r,\tau_F)=r^2F(r,\tau_F=0)+f^{\text{1-loop}}(r,\tau_F), \tag{23}$$

$$f^{\text{1-loop}}(r,\tau_F)=r^2F^{\text{1-loop}}(r,\tau_F)-r^2F^{\text{1-loop}}(r,\tau_F=0), \tag{24}$$

where $r^2F(r,\tau_F=0)$ is the static force at a given order at zero flow time, and $r^2F^{\text{1-loop}}$ is the full one-loop expression in Eq. (15). In this way, we correct for the change of the force due to the flow time up to one-loop order. The accuracy of the flow-time correction is consistent with the three-loop accuracy of the zero-flow-time part, as long as the flow-time correction subleading to $\alpha_s^2\tau_F/r^2$ is small compared to α_s^4. This appears to be the case in our study, where we invoke the restriction $\tau_F/r^2\lesssim 0.05$.

For the rest of the paper, we refer to Eq. (23) when dealing with the flowed static force at higher orders. We label the one-loop-order force [next-to-leading order (NLO)] as F1l, the two-loop force [next-to-next-to leading order (N^{2}LO)] as F2l, the two-loop force with leading ultrasoft logarithms resummed [next-to-next-to-leading logarithmic order (N^{2}LL)] as F2lLus, the three-loop force [next-to-next-to-next-to-leading order (N^{3}LO)] with F3l, and the three-loop force with leading ultrasoft logarithms

resummed as F3lLus. For the reasons discussed in [15], we also restrict the present study to the F3lLus force, although the force at three-loop order with next-to-leading ultrasoft logarithms resummed [next-to-next-to-next-to-leading logarithmic order (N^3LL)] would be available.

D. The force on the lattice

The Wilson loops $W_{r\times T}$ are constructed as the closed, path-ordered product of link variables, consisting of two straight spatial Wilson lines in the spatial plane separated by T in the temporal direction. The spatial Wilson lines have the length r in the direction $\hat{\mathbf{r}}$. The ends of both spatial Wilson lines are connected by two straight temporal Wilson lines. The static force can be obtained as the numerical derivative of Eq. (1) from the symmetric finite difference

$$F_{\partial V} = \frac{V(r+a) - V(r-a)}{2a}. \tag{25}$$

Other methods of defining the derivative of Eq. (1) consist, for example, in using the derivative of interpolating functions; these methods, however, add additional systematic uncertainties.

The main purpose of this work is to obtain the static force directly by computing $PW_{r\times T}gE_j(\mathbf{r} = r\hat{\mathbf{j}}, t^*)$, which consists of inserting a discretized jth chromoelectric field component into the path-ordered product at the temporal position t^* in one of the temporal Wilson lines. In general, t^* is arbitrary. Nevertheless, we choose $t^* = T/2$ for even-spaced separations, and an average over $t^* = T/2 \pm a/2$ for odd-spaced separations. This reduces the interactions between the chromoelectric field and the corners of the Wilson loop. We use the clover discretization for the field-strength tensor,

$$a^2F_{\mu\nu} = \frac{-i}{8}(Q_{\mu\nu} - Q_{\nu\mu}), \tag{26}$$

$$Q_{\mu\nu} = U_{\mu,\nu} + U_{\nu,-\mu} + U_{-\mu,-\nu} + U_{-\nu,\mu} = Q^\dagger_{\nu\mu}, \tag{27}$$

where $U_{\mu\nu}$ is a plaquette in the $\mu-\nu$ plane. This symmetric definition of the chromoelectric field corresponds to the symmetric center difference according to Eq. (25) at tree level. Finally, we replace $a^2F_{\mu\nu}$ with $a^2F_{\mu\nu} - \mathbb{1}\mathrm{Tr}(a^2F_{\mu\nu})/3$, which makes the components of the field-strength tensor traceless and corresponds to an a^2 improvement [44]. The chromoelectric field components are accessible through the components $a^2E_i = -a^2F_{i,4}$.

The direct determination of the force F_E on the lattice follows from Eq. (6) and the discretized version of $PW_{r\times T}gE_j(\mathbf{r} = r\hat{\mathbf{j}}, t^*)$. The finite extent of the chromoelectric field through its discretization introduces additional self-energy contributions with a nontrivial lattice spacing dependence. These self-energy contributions slow down the convergence to the continuum limit; they have been studied in lattice perturbation theory [45]. They are absent in the force obtained through the derivative, $F_{\partial V}$. Since both calculations provide the same physical quantity, we may set

$$Z_E F_E(r) = F_{\partial V}, \tag{28}$$

where the constant Z_E reabsorbs the additional self-energy contributions at finite lattice spacing. If $Z_E = 1$, no self-energy contributions are present, and we can assume that the quantity behaves in a trivial way in the continuum limit. Z_E from the static force was investigated non-perturbatively in a former study [28], and it was found that Z_E has only a weak r dependence. For a different discretization of the chromoelectric field insertion needed for determining transport coefficients, the renormalization constant Z_E was computed up to NLO in lattice perturbation theory [46]. More recent studies [47,48] rely on the gradient flow method to renormalize the field insertions. In this study, we also use gradient flow to show the renormalization property explicitly, and to improve the signal-to-noise ratio. In the rest of this work, the default force measurement is given in terms of the chromoelectric field—i.e., $F \equiv F_E$—while we still call the force obtained from the derivative of the static energy $\partial_r V \equiv F_{\partial V}$.

III. LATTICE SETUP AND TECHNICAL DETAILS

On the lattice, we measure $a^2F(t, r, T)$, which, multiplied by r^2/a^2, yields the dimensionless quantity $r^2F(t, r, T)$. We have data on a periodic $N_s^3 \times N_t$ (N_s: spatial lattice extent, N_t: temporal lattice extent) grid; in our case, the available grids are $20^3 \times 40$, $26^3 \times 52$, $30^3 \times 60$, and $40^3 \times 80$. Table II shows our lattice parameters. We use the scaling from [4], which is based on the scale r_0, to fine-tune the simulation parameters. With this scaling, our lattices share a physical size of approximately $(1.2\ \mathrm{fm})^3 \times 2.4\ \mathrm{fm}$. We produce the lattice configurations using over-relaxation and heat-bath algorithms with Wilson action and periodic boundary conditions.

We solve the gradient flow equation (12) with a fixed step-size integrator for the coarsest lattice ($20^3 \times 40$) and an adaptive step-size integrator for the finer lattices. In all

TABLE II. The parameters for the lattice ensembles. The scale t_0 was set on a smaller subset of lattice configurations.

N_S	N_T	β	a [fm]	t_0/a^2	N_{conf}	Label
20^3	40	6.284	0.060	7.868(8)	6000	L20
26^3	52	6.481	0.046	13.62(3)	6000	L26
30^3	60	6.594	0.040	18.10(5)	6000	L30
40^3	80	6.816	0.030	32.45(7)	3300	L40

gradient flow integrations, we use the Symanzik action. We measure pure Wilson loops and loops with chromoelectric field insertions. That way, we can determine both the static potential and its numerical derivative for obtaining the static force, and the force directly. In Appendix B, we show briefly the impact of gradient flow on the bare Wilson loops with and without chromoelectric field insertions. To find the reference scale t_0, we use the clover discretization in Eq. (26) to measure $\langle E \rangle$ and solve Eq. (11) for t_0. We use this reference scale to express our quantities r and τ_F in units of $\sqrt{t_0}$ and t_0, respectively, and to perform the continuum limit as $a^2/t_0 \to 0$.

The adaptive step-size integrator changes the gradient flow step sizes after every integration step, dependent on the lattice configuration. This means that the lattice measurement is done at different flow-time grids for each individual lattice configuration. Therefore, we need to interpolate the data to a common flow-time grid among the different lattice configurations. We use simple spline interpolations, since the gradient flow is a continuous transformation of the fields that produces a continuous function of the flow time. The interpolation can be done to a fixed flow-time grid in physical units, or to a fixed flow-time-ratio τ_F/r^2 grid. Data along a flow-time grid in physical units at a given fixed r can be easily presented on a flow-time-ratio axis by setting the x axis to τ_F/r^2.

We check the fluctuation of the topological charge and observe no full freezing of the topology. At our largest lattice (L40), the fluctuation of topology slows down, which increases the autocorrelation times of the topological charge. We inspect the autocorrelation of the L40 lattice more closely in Appendix C. The static energy (and consequently, its derivative) is known to be less affected by topological slowing down [49] than a bare gradient-flow-coupling measurement would be [50]. However, to be safe, we block our data such that the block size is larger than the topological autocorrelation times we see on any of the ensembles and settle for 30 jackknife blocks per ensemble. While the static force measurement is only weakly correlated with the topological charge, the scale t_0 can have a stronger dependence on it. To counter this, we measure t_0 only on a subset of configurations, having longer Monte Carlo time in between the measurements.

We have performed the simulations at a constant physical box size and have not tested for finite-volume effects from varying the physical volume. In [51], the finite-volume effects were studied and found to be minimal for hybrid static energies for almost the same set of lattice parameters. We expect the finite-volume effect to be equally small for the static force.

IV. PREPARATORY ANALYSES

In this section, we analyze and prepare the raw lattice data, and we perform the continuum limits needed for the Λ_0 extraction. This preparation contains the plateau extraction for the static energy and the $T \to \infty$ limit for the direct force measurement, which is covered in Sec. IV A. Renormalization properties of gradient flow are discussed in Sec. IV B, followed by the continuum extraction, worked out in Sec. IV C. To finalize this section, we investigate the behavior of the various scales r_0, r_1, and t_0.

A. Plateau extraction

We extract the plateaus in the $T \to \infty$ limit based on a procedure from [52] that relies on an Akaike information criterion. We summarize it here briefly. This procedure is applied to data at every fixed r and τ_F combination for each lattice ensemble.

In the first step, we perform constant fits for all possible continuous ranges within $T/a = 1$ and a certain $T_{\max}$ with a minimum of at least three support points, each fit minimizing χ^2 as

$$\mathbf{a}^{\star}_{i_1,i_2} = \underset{\mathbf{a}_{i_1,i_2}}{\operatorname{argmin}} \chi^2(\mathbf{a}_{i_1,i_2}) = \underset{\mathbf{a}_{i_1,i_2}}{\operatorname{argmin}} \sum_{i,j=i_1}^{i_2} \big(f(x_i, \mathbf{a}_{i_1,i_2}) - y_i\big) \times C^{-1}_{i,j} \big(f(x_j, \mathbf{a}_{i_1,i_2}) - y_j\big), \tag{29}$$

where i_1 and i_2 are the indices defining the specific lower and upper limits of the range; f represents the model function, which, in our case, is the constant function $f(x, \mathbf{a}) = a_0$; and $\mathbf{a}$ is the parameter vector, which consists of only one component for the constant fit. The dataset D is specified by y_i, the force measurement at $T = x_i$, and C_{ij} is the covariance matrix along the T axis.

In the next step, we define, for a given fit and for a specific range i_1 to i_2, the Akaike information criterion (AIC) as

$$\mathrm{AIC}_{i_1,i_2} = \chi^2(\mathbf{a}^{\star}_{i_1,i_2}) + 2k + 2(i_1 - i_2), \tag{30}$$

where k is the number of parameters of the fit function, $k = 1$ for the constant fit, and $i_1 - i_2$ is the relative number of discarded data points within the total range. In theory, we are required to have the absolute number of discarded data points, which is given by $N_{\mathrm{tot}} - (i_1 - i_2)$; however, this corresponds to a global shift for all AIC values, which can be eliminated in the next step.

In the third step, we find the model probability of a specific fit range as

$$p(i_1, i_2|D) = \frac{1}{Z} \exp^{-\frac{1}{2}\mathrm{AIC}_{i_1,i_2}}, \tag{31}$$

where Z is a normalization constant such that the sum of the probabilities over all considered fit ranges reduces to 1:

$$\sum_{i_1<i_2} p(i_1, i_2|D) = \frac{1}{Z} \sum_{i_1<i_2} \exp^{-\frac{1}{2}\mathrm{AIC}_{i_1,i_2}} \overset{!}{=} 1. \tag{32}$$

At this stage, we observe that a global shift of all AIC values has no effect on the model probability, since it is absorbed into a redefinition of Z. Thus, we perform the global shift $\mathrm{AIC}_{i_1,i_2} \to \mathrm{AIC}_{i_1,i_2} - \min_{i_1,i_2}\mathrm{AIC}_{i_1,i_2}$, because it makes the computations of the model probability on the most important ranges numerically more stable.

In the last step, we compute model expectation values and deviations with the given model probabilities. The final results and their deviations from the plateau fit are thus given by

$$\dot{a}_n = \langle a_n \rangle = \sum_{i_1,i_2} a^{\star}_{n,i_1,i_2} p(i_1, i_2|D), \tag{33}$$

$$\sigma_n^2 = \langle (a_n - \bar{a}_n)^2 \rangle = \langle a_n^2 \rangle - \langle a_n \rangle^2. \tag{34}$$

This procedure can be generalized to more complex model functions, which we use in this work for the continuum limit and the Λ_0 extraction. Furthermore, to achieve a better understanding of the process, we compute the average fit ranges

$$\langle x_{i_1} \rangle \equiv \sum_{i_1,i_2} x_{i_1} p(i_1, i_2|D), \tag{35}$$

$$\langle x_{i_2} \rangle \equiv \sum_{i_1,i_2} x_{i_2} p(i_1, i_2|D) \tag{36}$$

and their deviations, defined equivalently to Eq. (34).

A crucial part of this procedure is the selection of a certain $T_{\max}$. In principle, $T_{\max}$ can be chosen to cover the whole temporal range of the Wilson loops, since the information criterion should eventually select the important ranges. However, especially at larger T, the statistical errors for the covariance matrix are underestimated. These give inaccurate model probabilities for insignificant fit ranges. Therefore, we have to select a proper $T_{\max}$ value to prevent this behavior. To find a suitable $T_{\max}$, we perform the whole procedure for several $T_{\max}$ values and select the one where, for a small variation of $T_{\max}$, the final result stays invariant. This is justified by the assumption that the important fit ranges, selected by the information criterion, should be fully captured by $T_{\max}$. Hence, a small variation of $T_{\max}$ should not modify the important fit ranges. The $T_{\max}$ selection can be automatized by taking data up to a $T_{\max}$ where the relative statistical error is less than 10%, and then decreasing $T_{\max}$ iteratively until an invariant range of $T_{\max}$ is found. However, the automatized procedure does not work in every case, and sometimes a selection has to be made manually. To do so, it is enough to identify a representative selection of a few flow times and distances r, and use piecewise linear interpolations to cover the whole dataset.

The Akaike information procedure also provides us an error estimate of the plateau extraction. Nevertheless, to propagate the statistical error, we use jackknife resampling with 30 blocks and perform the plateau extraction for every jackknife block. If the resulting jackknife error is comparable with the fit error, we use only the jackknife samples to propagate the error. In several cases, however, the choice of the fit range is a significant systematic error source, and we need to take it into account. In these cases, we label the systematic error by the Akaike information criterion of the corresponding observable as σ^2_{AIC}, and the statistical error as σ^2_{stat}.

B. Implications of the gradient flow

Gradient flow has an impact not only on the signal-to-noise ratio improvement, but also on reducing discretization effects that occur through self-interaction contributions. Therefore, we are also interested in the renormalization factor Z_E of the chromoelectric field insertion from Eq. (28). We find Z_E nonperturbatively by solving Eq. (28) for Z_E, which gives the ratio of the numerical derivative of the static potential and the direct force measurement according to Eq. (6):

$$Z_E(r) = \frac{\partial_r V(r)}{F(r)}. \tag{37}$$

In [28], it was shown that $Z_E(r)$ has a weak r dependence. Hence, we extract Z_E as a plateau fit, similar to the $T \to \infty$ limit discussed in Sec. IV A, over r at fixed τ_F; we keep r approximately between $0.3r_0$ and $0.65r_0$. Figure 1 shows the result for Z_E for all lattice sizes against the flow time. At minimal flow times, we obtain that $Z_E > 1$, meaning that at minimal flow times, the direct force measurement is affected by self-energy contributions originating from the chromoelectric field discretization. Furthermore, we obtain that $Z_E = 1$ within 1% deviation for flow radii larger than one lattice spacing, which is required for reliable continuum

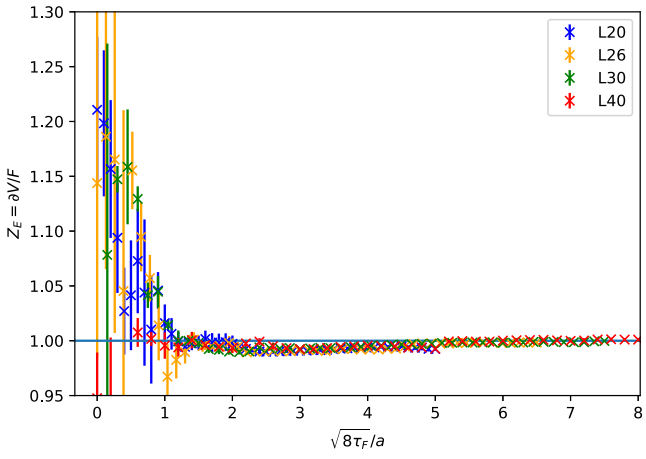

FIG. 1. Z_E for all lattice sizes with increasing flow time. We see that for flow radii larger than one lattice spacing, the factor Z_E becomes practically 1.

limits. We recognize a small bump within the 1% range for flow radii within $1.5 < \sqrt{8\tau_F}/a < 5$ for all lattice sizes. This is expected, as the $\partial_r V(r)$ part is a simple finite difference and hence only approximates the static force. We observe that this systematic difference between the definitions of the force seems to vanish at larger flow radii ($\sqrt{8\tau_F}/a > 6$). In conclusion, we find that a minimum amount of flow time ($\sqrt{8\tau_F} > a$) has to be applied to be in the regime where the gradient flow has practically eliminated the nontrivial discretization effects.

C. Continuum extrapolation

1. Continuum interpolation

Preparing for the continuum limit, we interpolate r^2F on all ensembles at a fixed flow time to a common r range in $\sqrt{t_0}$ units. We use polynomial interpolations at different orders:

$$P_n(r) = \sum_{k=0}^{n} a_{k,n} r^k, \tag{38}$$

with $a_{k,n}$ being the coefficients. We have different coefficients for different fixed-order polynomials. An interpolation at fixed order corresponds to a single fit, where we minimize the χ^2.

In addition, interpolations have the advantage that small fluctuations within the data get smoothed. Polynomial interpolations can have fluctuations, especially higher-order polynomial fits, and hence, we average over different polynomial orders to reduce those fluctuations:

$$P_{\text{inter}}(r) = \sum_{n=n_{\min}}^{n_{\max}} w_n P_n(r), \tag{39}$$

$$\sum_{n=n_{\min}}^{n_{\max}} w_n = 1, \tag{40}$$

where w_n are normalized, adjustable weights.

For the L20, L26, and L30 lattices, we use equal weights for all polynomial orders. We choose polynomials of orders $n = 4, 5, 6, 7$ for L20; orders $n = 7, 8, 9, 10$ for L26; and orders $n = 8, 9, 10, 11$ for L30. For L40, we use an Akaike average [52] over the orders from 4 to 12, because at some flow times the plateau extraction at larger r gives fluctuating results. This results from underestimated systematic effects and causes a change in the effective polynomial orders, which is considered through the Akaike average. The weights are found analogously to Eqs. (30) and (31) through

$$\text{AIC}_n = \chi^2_n + 2\,\text{d.o.f.}, \tag{41}$$

$$w_n \propto e^{-\frac{1}{2}\text{AIC}_n}, \tag{42}$$

where the final values of w_n are fixed by the normalization condition. To propagate the statistical error, the continuum interpolation is done for every jackknife block.

This procedure works for most of the data. An exception is the data at small r (up to $r/a = 3$) for the L26 lattice. We obtain a miscarried interpolation in this case due to large-r effects in the interpolation. For the L26 lattice, it turns out that spline interpolations up to $r/a = 3$ and changing to the polynomial interpolation for larger r works properly.

2. Tree-level improvement

To reduce the effects of finite lattice spacings, we apply a tree-level improvement procedure to the data at finite flow time by dividing out the leading lattice perturbation theory result. Following [53], the static energy in lattice perturbation theory at finite flow time can be written as

$$V_{\text{lat}}(r,\tau_F) = -C_F g^2 \int \frac{\mathrm{d}^3\mathbf{k}}{(2\pi)^3} e^{i\mathbf{k}\cdot\mathbf{r}} e^{-2\tau_F D^{-1}_{\text{GF}}} D_{\text{MC}}, \tag{43}$$

where we have assumed $a = 1$ for simplicity and D is the lattice propagator:

$$D^{-1} = 4\sum_{i=1}^{4}\left(\sin^2\frac{k_i}{2} + c_w \sin^4\frac{k_i}{2}\right), \tag{44}$$

with $c_w = 0$ for the Wilson action, which we use for the simulation part, D_{MC}, and $c_w = 1/3$ for the Symanzik action, which we use in the gradient flow equations, D_{GF}. Similarly to the zero-flow-time case that was derived in [28], the static force coming from the chromoelectric field insertion reduces to a symmetric finite difference:

$$F_{\text{lat}}(r,\tau_F) = \frac{V_{\text{lat}}(r+a,\tau_F) - V_{\text{lat}}(r-a,\tau_F)}{2a}. \tag{45}$$

Now, we can tree-level-improve the measured force F_{meas} by dividing out the leading lattice expression and multiplying by the continuum tree-level gradient flow expression:

$$F_{\text{improved}}(r,\tau_F) = \frac{F^{\text{tree-level}}_{\text{cont}}(r,\tau_F)}{F_{\text{lat}}(r,\tau_F)} F_{\text{meas}}(r,\tau_F), \tag{46}$$

where $F^{\text{tree-level}}_{\text{cont}}$ is defined as the $\mathcal{O}(\alpha_S)$ contribution to Eq. (15).

3. Continuum extrapolation

We use the interpolated and tree-level improved data for the continuum limit, which is obtained from extrapolations linear and quadratic in a^2/t_0 at fixed physical distances r and fixed physical flow times τ_F:

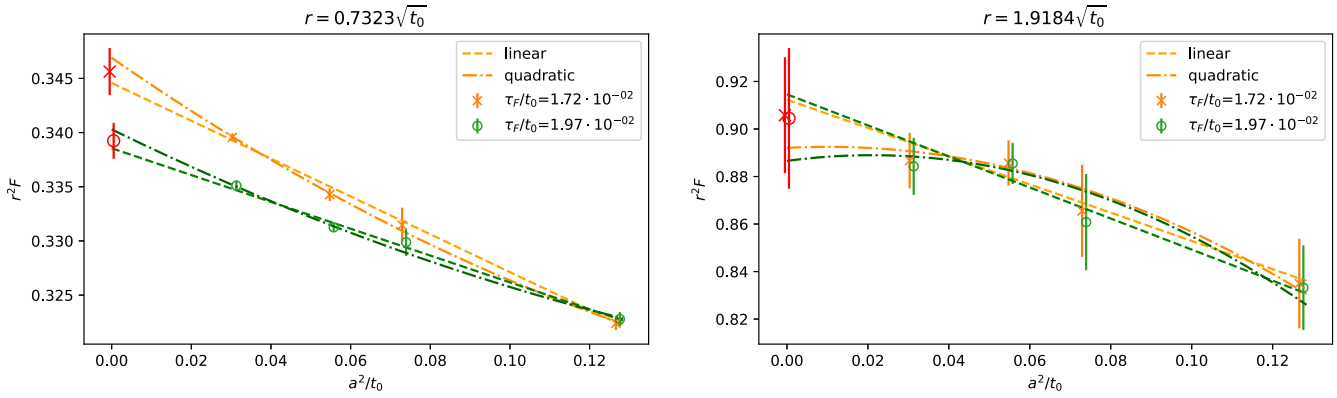

FIG. 2. Examples of continuum extrapolation for two different separations r. The figure shows the linear and quadratic continuum limits: the line corresponds to the linear limit, and the curve to the quadratic one.

$$f^{\text{linear}}(a^2/t_0) = m\frac{a^2}{t_0} + c_l, \tag{47}$$

$$f^{\text{quadratic}}(a^2) = A\frac{a^4}{t_0^2} + B\frac{a^2}{t_0} + C_l, \tag{48}$$

where m, c_l, A, B, and C_l are the fit parameters, and c_l and C_l are the continuum limits of the linear and quadratic extrapolations, respectively. We take an Akaike average, defined for polynomials as in Eqs. (41) and (42). Figure 2 shows a working example for the continuum limit at two fixed distances r and for each distance at two different flow times.

Although we use tree-level improved data and Akaike average over linear and quadratic continuum limits, often both χ^2/d.o.f.'s are too large. Hence, we restrict to data which accomplish that at least one of the extrapolations gives $\chi^2/\text{d.o.f.} < 3.0$, and that the flow radius fulfills $\sqrt{8\tau_F} > a$. The remaining, filtered data represent reliable continuum limit results, with which we continue the further analyses.

D. r_0 and r_1 scales

In terms of the force $F(r)$, we define a reference scale as

$$r^2F(r,\tau_F)|_{r(c,\tau_F)} = c, \tag{49}$$

with a dimensionless number c. Common choices are $r_0(\tau_F) \equiv r(c = 1.65, \tau_F)$, $r_0 \equiv r_0(\tau_F = 0)$ [6], and $r_1(\tau_F) \equiv r(c = 1, \tau_F)$, $r_1 \equiv r_1(\tau_F = 0)$ [54]. In the original proposals, the scales $r(c)$ are defined with the force at zero flow time; however, in our case, the force is computed at different flow times. Thus, we obtain flow-time-dependent r_0 and r_1 as shown in Figs. 3 and 4. To find r_0 and r_1, we perform multiple polynomial interpolations of $r^2F(r,\tau_F)$ for larger r values along the r axis and at fixed flow-time ratio τ_F/r^2, and we find the roots of the individual interpolations as $(r^2F)^{\text{inter}} - c = 0$. The final scales are given in terms of an Akaike average over the roots of the polynomial interpolators.

Both scales, r_0 and r_1, approach a constant plateau within a recognizable flow-time regime and start deviating from this plateau at larger flow times. We perform plateau

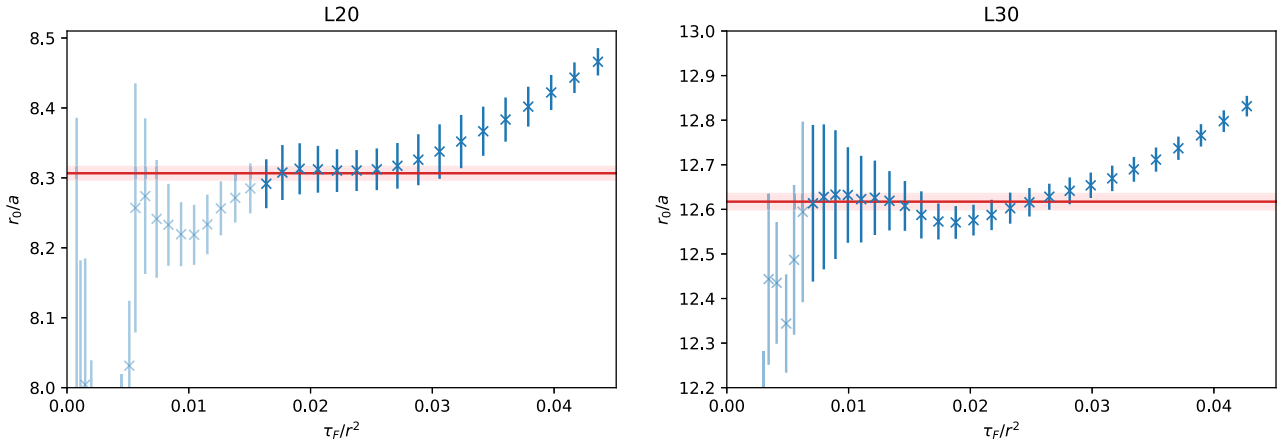

FIG. 3. The r_0 scale along the flow-time axis.

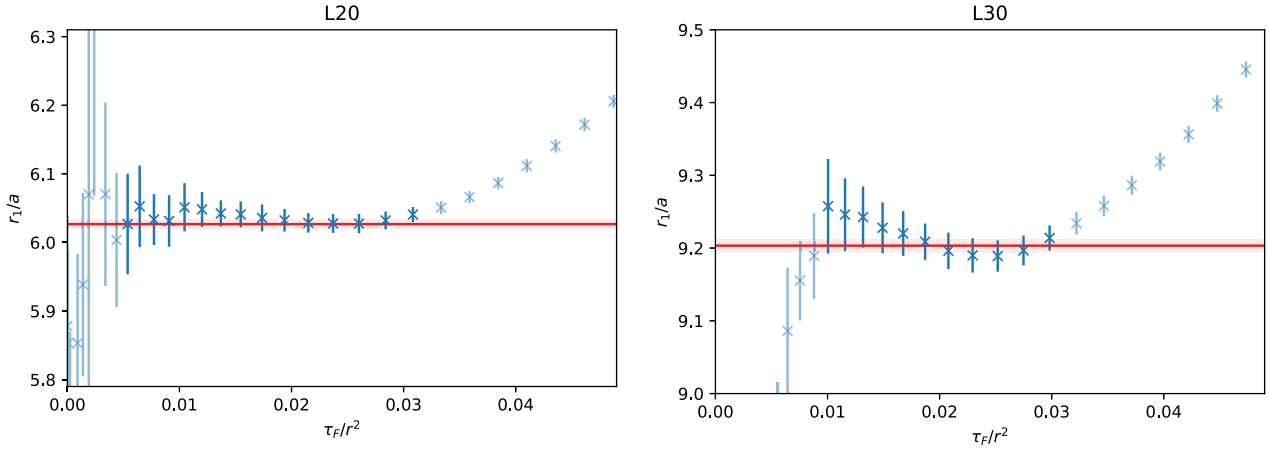

FIG. 4. The r_1 scale along the flow-time axis.

fits within this range for a zero-flow-time extraction of both scales, and we find them comparable to the scales fixed by [4]. The results are shown in Table III. We see that the error of the scale setting is dominated by the statistical fluctuation rather than by the Akaike error of the polynomial interpolators.

The ratio of the two scales, $r_0(\tau_F)/r_1(\tau_F)$, is shown in Fig. 5. We take the a^2/t_0 continuum limit followed by a constant zero-flow-time limit. Finally, we obtain

$$\frac{r_0}{r_1} = 1.380(14). \tag{50}$$

To our knowledge, there are no prior direct determinations of the scale ratio r_0/r_1 in pure gauge. However, in Ref. [55], this ratio was roughly estimated to be ∼1.37 based on the curves shown in [4], which agrees well with our extraction within errors. The extracted value is about 9% larger than the ratio in unquenched theories with $2+1$ or $2+1+1$ fermion flavors [1,47]. Such a shift is to be expected, due to the effect of unquenching the quark flavors. A similar effect between quenched and unquenched scales has been seen for the gradient-flow scale ratios in Ref. [56].

We repeat the same procedure for the ratios $\sqrt{8t_0}/r_0$ and $\sqrt{8t_0}/r_1$. Figure 6 shows an example for the ratio $\sqrt{8t_0}/r_0$. The final results for the ratios of the scales are

TABLE III. Results for r_0 and r_1 in the zero-flow-time limit at finite lattice spacing. The table includes the statistical error ("stat" subscript), the systematic error by choosing different fit ranges ("AIC" subscript), and the errors added in quadrature.

	r_0/a	σ_{stat}	σ_{AIC}	$\sigma_{\text{stat+AIC}}$	r_1/a	σ_{stat}	σ_{AIC}	$\sigma_{\text{stat+AIC}}$
L20	8.306	0.017	0.010	0.020	6.026	0.0090	0.006	0.011
L26	10.833	0.031	0.025	0.040	7.849	0.014	0.010	0.018
L30	12.617	0.032	0.018	0.040	9.203	0.0130	0.008	0.015
L40	16.933	0.042	0.015	0.044	12.316	0.0280	0.011	0.030

$$\frac{\sqrt{8t_0}}{r_0} = 0.9569(66), \tag{51}$$

$$\frac{\sqrt{8t_0}}{r_1} = 1.325(13). \tag{52}$$

Our extracted ratio $\sqrt{8t_0}/r_0$ agrees within errors with the previous determinations [31,57–63],[1] albeit the mean value is slightly above most of the existing results. We show the comparison to the existing literature in Fig. 7. The previous results are somewhat correlated, since most of them focus on t_0 calculation and use the data from Refs. [4,5] for at least part of their dataset for r_0. Again, the quenched ratios are larger than the unquenched ones [1], as has been previously seen in Ref. [56]. To our knowledge, this is the first direct measurement of the scale ratio $\sqrt{8t_0}/r_1$ in pure gauge.

V. ANALYSES OF THE CONTINUUM RESULTS

After having worked out the continuum limit in Sec. IV C, we compare the lattice results with the perturbative expressions to extract Λ_0. Since gradient flow introduces another scale next to $1/r$, we have several possibilities to compare the lattice results with the perturbative expressions. In the first approach, we use the simple expression of the flowed force in Eq. (22), which turns out to be also applicable to large-r results. In the second approach, we compare the lattice results either by keeping the scale $1/r$ fixed and inspecting the behavior along the flow time, or vice versa, by keeping τ_F fixed and inspecting the behavior along the distance r. We show plots only for the perturbative one-loop (F11) and three-loop with leading ultrasoft resummation

[1]The FlowQCD result from Ref. [57] is inferred from their results of $\sqrt{t_0}/w_0$ and r_0/w_0, neglecting error correlation. Therefore, the error shown in Fig. 7 is certainly overestimated.

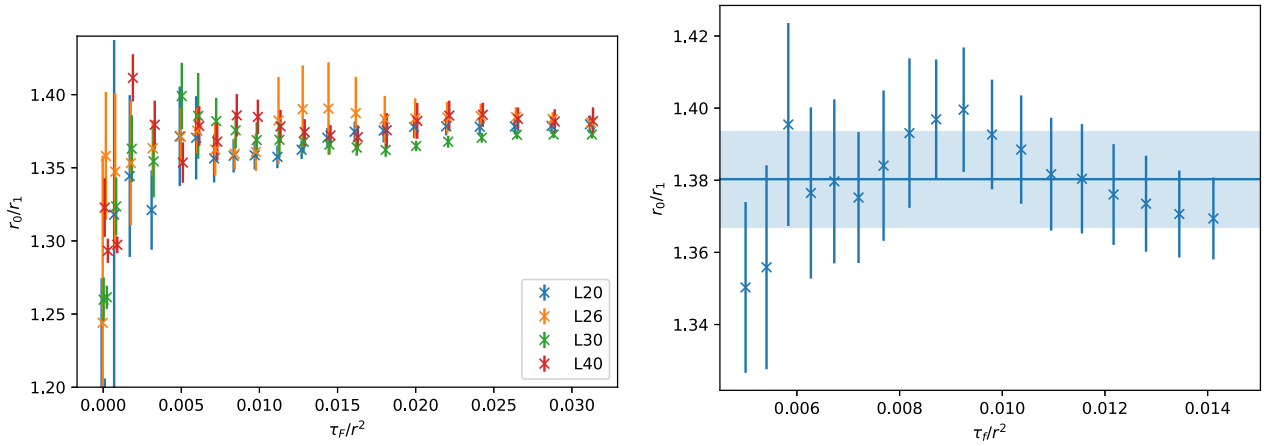

FIG. 5. The ratio of the scales r_0 and r_1. The left side shows the ratio at finite lattice spacing; the right side shows the continuum limit with the constant zero-flow-time extraction.

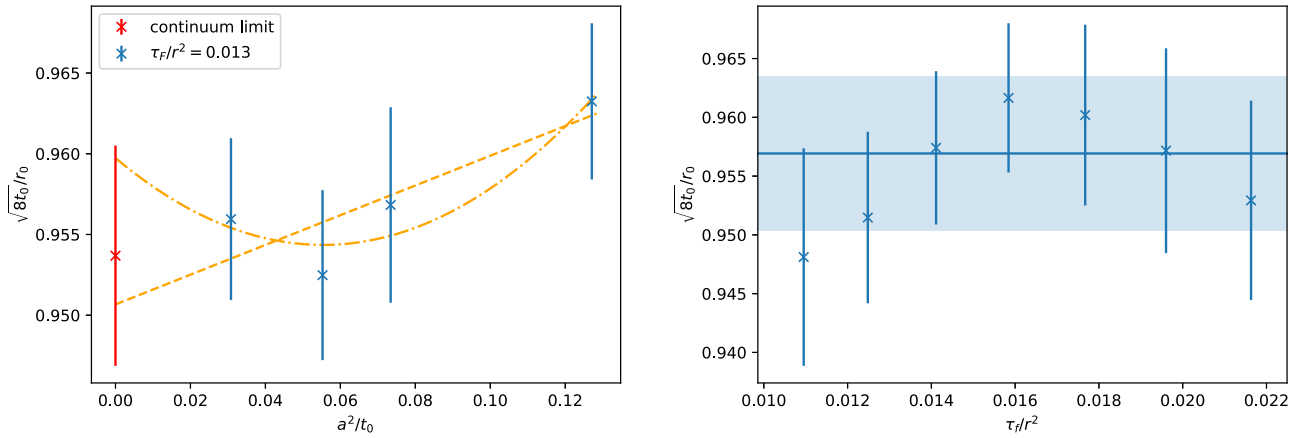

FIG. 6. Left: An example for the continuum limit of the ratio $\sqrt{8t_0}/r_0$ at a fixed flow-time ratio. The straight line corresponds to a continuum limit linear in a^2/t_0, and the curved line corresponds to a polynomial up to quadratic order in a^2/t_0. The red cross and bar shows the final continuum limit of a weighted average of both extrapolations. Right: The flowed continuum ratio with the constant zero-flow-time limit.

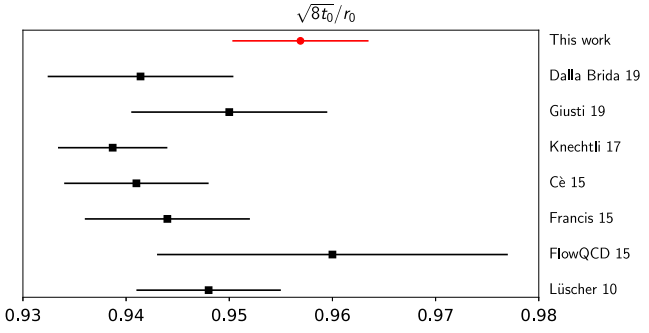

FIG. 7. Our extracted ratio (red circle) of the scale ratio $\sqrt{8t_0}/r_0$ compared to the existing results (black squares) in the literature.

(F3lLus) expressions; however, in the result tables, we also provide extractions based on the two-loop with and without leading ultrasoft resummation (F2l and F2lLus), and based on three-loop without ultrasoft resummation (F3l) expressions.

A. Constant zero-flow-time limit at fixed r

We know from Eq. (22) that the static force has a constant behavior at small flow times. Physical quantities are defined at zero flow time; hence, we need to perform the zero-flow-time limit, $\tau_F \to 0$, while we keep r fixed. In the constant regime, we perform this by a constant fit at fixed distance r. Figure 8 shows data where we obtain a constant behavior of the flowed force. The left side shows the data for the smallest r before the smaller flow time comes into conflict with the $\sqrt{8\tau_F} > a$ condition. The right side shows

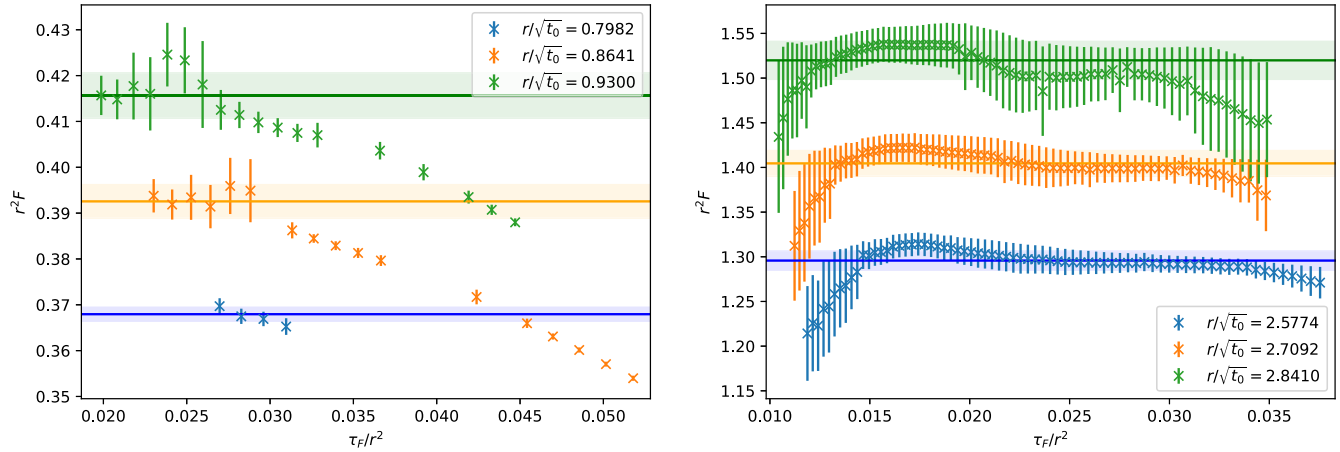

FIG. 8. Examples of the flowed force in a regime where a constant behavior can be obtained. The left side shows the data for the smallest r where a constant regime can be obtained. The right side shows the flowed force at larger r, where we can apply a constant fit in a proper range of τ_F/r^2.

data at larger r values, where the condition $\sqrt{8\tau_F} > a$ is fulfilled at even minimal flow-time ratios. The small-flow-time expansion is performed in the ratio τ_F/r^2; thus, small flow time is defined in the sense of small-flow-time ratio, which is a dimensionless quantity. The condition $\sqrt{8\tau_F} > a$ is given in terms of flow times in physical units; hence, considering this condition in terms of ratio moves it to smaller flow-time ratios for larger r, since the r in the denominator decreases the ratio.

In Fig. 9, we see the final result of the constant zero-flow-time limits. We identify an increasing behavior with small errors up to $r/\sqrt{t_0} \approx 3.0$. Around the distance of $r/\sqrt{t_0} \approx 2.25$, we are faced with difficulty extrapolating to the continuum, and we obtain χ^2/d.o.f.'s of order 4 and larger.

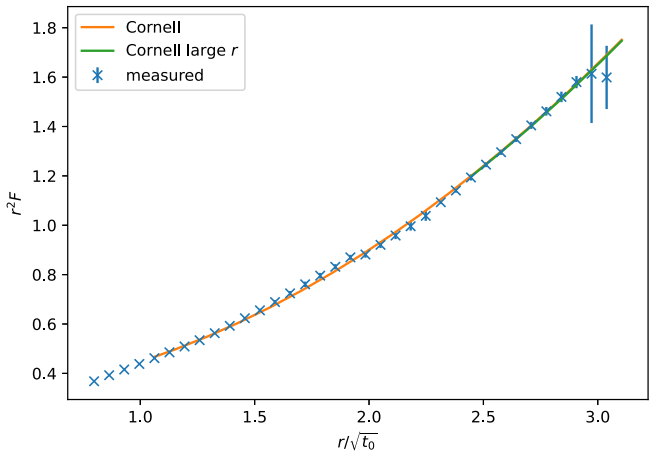

FIG. 9. The extracted force from the constant zero-flow-time limits with two Cornell fits. In a window from $r/\sqrt{t_0} \approx 2.1$ to $r/\sqrt{t_0} \approx 2.3$, the continuum limit turns out to be difficult to reach. We lose the signal at larger r around $r/\sqrt{t_0} \approx 3.0$.

We perform a Cornell fit to the data from $r/\sqrt{t_0} \approx 1.1$ to $r/\sqrt{t_0} \approx 3.0$, and we obtain

$$r^2F(r) = A + \sigma r^2, \tag{53}$$

$$A = 0.297(6), \tag{54}$$

$$\sigma t_0 = 0.151(3). \tag{55}$$

The string tension σ is a quantity that is dominated by the large-r regime; hence, in addition, we perform the fit only for data beyond the region where the continuum limits are problematic up to $r/\sqrt{t_0} \approx 3.0$. In this case, we obtain

$$A = 0.268(33), \tag{56}$$

$$\sigma t_0 = 0.154(6). \tag{57}$$

The uncertainty for A is 5 times larger now, which is to be expected, since it is a small r quantity. The results for σ from both ranges agree within their uncertainties. With the result in Eq. (51), we can express the string tension in r_0 units:

$$\sigma r_0^2 = 1.345(54). \tag{58}$$

In the past, the string tension was found to be $\sigma r_0^2 = 1.353(3)$ [64] at finite lattice spacing with $\beta = 6.0$, which is in good agreement with our result. Continuum results were obtained in [34,65] in another reference scale $\bar{r}$. With the ratio $\sqrt{8t_0}/\bar{r}$ from [34], these results become $\sigma t_0 = 0.133(2)$ and $\sigma t_0 = 0.143(2)$, respectively. Nevertheless, the ratio $\sqrt{8t_0}/\bar{r}$ in [34] is only an approximation over several lattice sizes, and it is not extrapolated to the continuum limit. Reliable continuum results for the string tension can be found in Refs. [66,67] in units of the critical

temperature T_c. With the conversion factor $T_c\sqrt{t_0}$ from [58], these results become $\sigma t_0 = 0.1484(22)$ and $\sigma t_0 = 0.156(3)$, which agree well with our result.

At small r, we extract Λ_0 from the data by fitting the perturbative force at the available orders. We solve the renormalization group equation for the running of the coupling α_s numerically by using the RunDec package [68–70], which takes Λ_0 as an input parameter. Setting the scale μ to a specific choice, we remain with a fit function depending solely on the parameter Λ_0, which serves as the fit parameter. The perturbative coefficients can be found in the literature [19–24], and an explicit equation for the force can be found in Eqs. (10) and (11) of [15]. Figure 10 shows examples of the fit for two different orders. Table IV shows the fit results. We observe that the error is dominated by the statistical fluctuations rather than by the systematic uncertainty due to the choice of the fit ranges.

B. Flow-time behavior of the force at fixed r or fixed τ_F

In the very small-r regime, the requirement $\sqrt{8\tau_F} > a$ moves the data points along the τ_F/r^2 axis outside the regime where they are flow-time independent even for the smallest possible flow time. Therefore, we compare the lattice data with the full expression of the force, Eq. (23)—i.e., without expanding for small τ_F.

We inspect the small-r flow-time behavior first at fixed distances r, which corresponds to the classical zero-flow-time limit. In a second approach, we fit along the r axis at fixed flow times to extract $\sqrt{8t_0}\Lambda_0$. Since the dependence on τ_F of the numerical extraction turns out to be negligible within the distance and flow-time regions used for the fits to the lattice data, getting $\sqrt{8t_0}\Lambda_0$ provides in practice its zero-flow-time limit.

TABLE IV. The fit result for $\sqrt{t_0}\Lambda_0$ from the constant zero-flow-time-limit extracted data at different orders. We see that the error is dominated by statistical fluctuations rather than the choice of the proper fit window.

Order	$\sqrt{8t_0}\Lambda_0$	σ_{stat}	σ_{AIC}	$\sigma_{\text{stat+AIC}}$
F1l	0.8214	0.0044	0.0018	0.0047
F2l	0.6635	0.0048	0.0029	0.0056
F2lLus	0.6961	0.0057	0.0039	0.0069
F3l	0.6197	0.0036	0.0024	0.0043
F3lLus	0.6353	0.0032	0.0013	0.0035

1. Fixed r

Figures 11 and 12 show the flow-time behavior of the force at two different fixed r values along the flow-time axis. We compare our lattice data with the perturbative expressions of the force at different orders and fit them to the data. Λ_0 serves as the fit parameter. In the figures, we show the fit results for the case of different, but fixed choices of b in Eq. (21). The fit range starts at the smallest possible flow time. For the upper bound, we take an Akaike average [52] over different fit ranges to reduce the systematics due to the fit range choice.

From the figures, we get that the choice of the scale parameter b has a definitive effect on how well the perturbative curve describes the data. A value of $b = 1$ guarantees the correct asymptotic behavior at large flow time [37]. However, we see that $b = 1$ is the worst of our b choices at describing the actual lattice data in the range of flow times we are interested in. Hence, we use negative values of b, which still lead to valid scaling in our range of flow times, as discussed in Appendix A. At small r (left-side plots in Figs. 11 and 12), the slope along the flow time is strong, while at the largest r to which we can reasonably apply fixed-r fits (right-side plots in Figs. 11 and 12), the

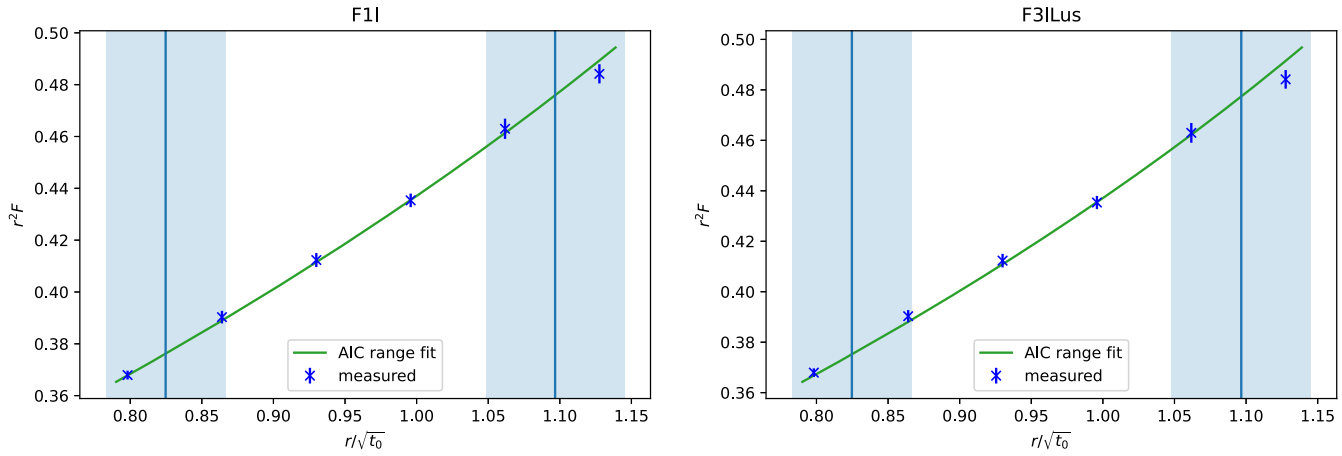

FIG. 10. The $\sqrt{8t_0}\Lambda_0$ extraction with constant zero-flow-time extrapolation at the smallest possible distances r. The vertical lines with the dimmer bar represent the lower and upper averaged fit range according to Eqs. (35) and (36).

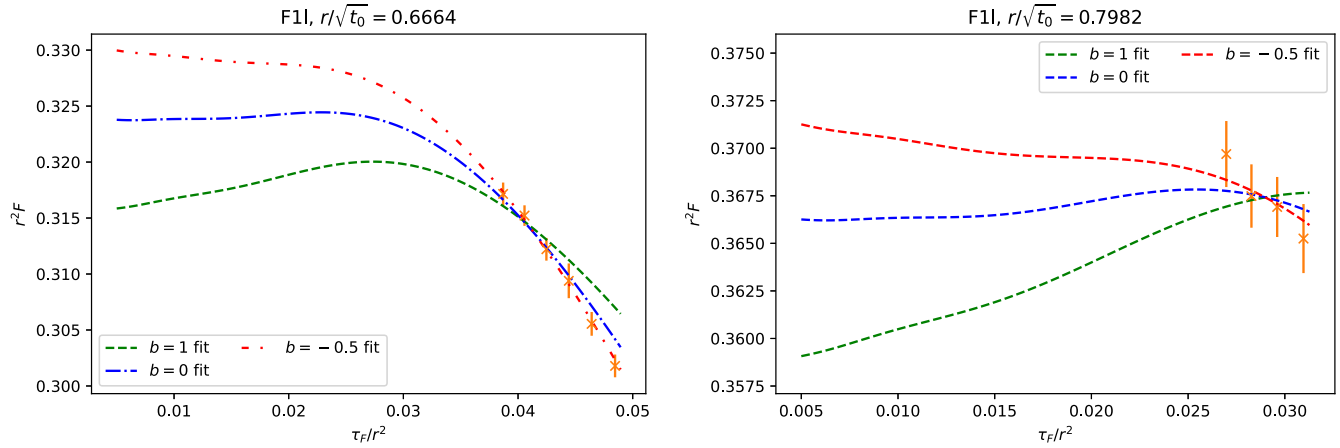

FIG. 11. Comparison of different zero-flow-time limits at one-loop order at fixed r. We compare fits with different scale choices obtained by varying b according to Eq. (21).

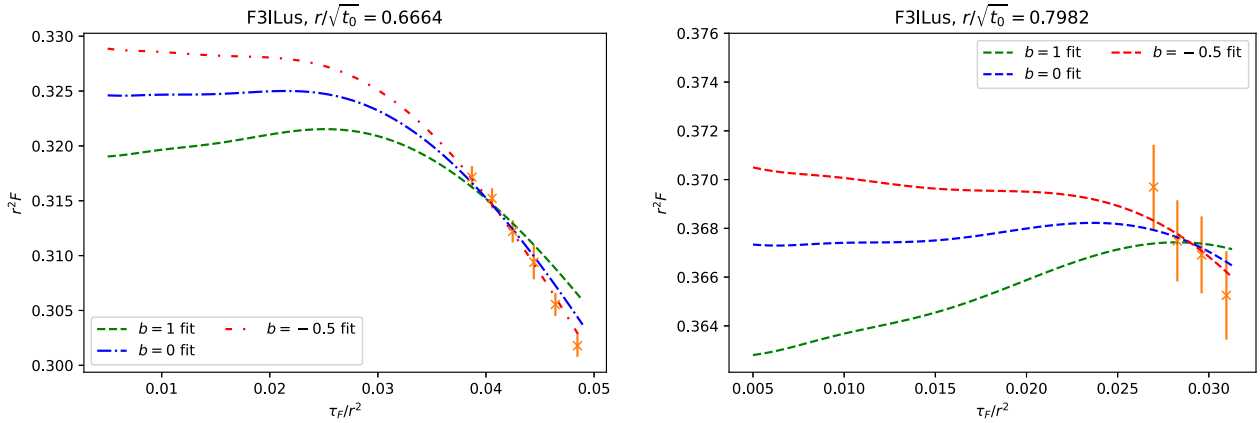

FIG. 12. As in Fig. 11, but with the fit function now being the force at three loops with leading ultrasoft resummation.

data points seem already sensitive to the constant behavior of the force expected at small flow times. At small flow times within our considered flow-time range, the fits with $b = 0$ and $b = -0.5$ agree reasonably well with the data. Table V shows an incomplete part of the fit results.

We conclude that for smaller r, which requires going to larger flow-time ratios τ_F/r^2, a negative value of b describes the data better in the large-flow-time regime than $b = 0$ or 1, whereas for larger r all choices might describe the data within the given uncertainties. That means that fixing b introduces another source of uncertainty which has to be considered. In the zero-flow-time limit, all choices of b give $\mu = 1/r$, which is the natural scale choice for the static force and energy at zero flow time.

2. Fixed τ_F

In the next step, we use data at fixed flow times τ_F and fit the perturbative force along the r axis. We use an Akaike average [52] over different fit windows for reducing systematics by choosing the right fit window. We perform one-parametric fits at fixed b for $\sqrt{8t_0}\Lambda_0$. Figure 13 shows an example fit for $b = 0, 1, -0.5$ for F1l and F3lLus at the same flow time. The left vertical line with the dimmer band corresponds to the average lower fit limit for the $b = 0$ fit, and the right vertical line to its average upper limit.

We observe that the $b = 0$ fit describes the data over a wide r range from small to larger r. The $b = 1$ fit describes the data around $r/\sqrt{t_0} = 1$ and up to larger r in the same way as the $b = 0$ fit, but it deviates from the data at smaller r in contrast to the $b = 0$ fit. This matches with its lower fit range limit being at larger r, but the upper fit range limit being the same as in the $b = 0$ fit, indicating that the effective fit range for $b = 1$ is more on the larger-r side. The $b = -0.5$ fit describes the data around $r/\sqrt{t_0} = 1$ like the $b = 0$ and $b = 1$ fits, but in contrast to the $b = 1$ case, it fits better to the data at small r and deviates from the data at larger r. This matches with its upper fit range limit being at smaller r, but the lower fit range limit being the same as in

TABLE V. Fit results at fixed r along the flow-time axis for three different choices of the perturbative order of the static force. We start at the smallest possible flow time and use an Akaike range fit for different upper limits. No value for σ_{AIC} indicates that there are not enough points along the flow time to perform an Akaike range fit. The given χ^2/d.o.f. corresponds to the most likely fit range. $\overline{\tau_F/r^2}_{\mathrm{Max}}$ gives the Akaike averaged upper flow-time limit.

Order	$r/\sqrt{t_0}$	b	$\sqrt{8t_0}\Lambda_0$	σ_{stat}	σ_{AIC}	χ^2/d.o.f.	$\overline{\tau_F/r^2}_{\mathrm{Max}}$
F3lLus	0.6664	1	0.6020	0.0030	0.0010	0.57	0.0449(9)
		0	0.6229	0.0031	0.0010	0.52	0.0463(16)
		−0.5	0.6388	0.0029	0.0005	0.22	0.0473(14)
	0.7323	1	0.6128	0.0037	0.0011	0.93	0.0381(14)
		0	0.6300	0.0037	0.0009	0.37	0.0395(20)
		−0.5	0.6427	0.0037	0.0004	0.21	0.0403(19)
	0.7982	1	0.6210	0.0036		0.72	
		0	0.6348	0.0037		0.39	
		−0.5	0.6440	0.0038		0.23	
F2l	0.6664	1	0.6132	0.0032	0.0010	0.59	0.0449(9)
		0	0.6361	0.0033	0.0011	0.51	0.0463(16)
		−0.5	0.6538	0.0031	0.0005	0.20	0.0474(14)
	0.7323	1	0.6274	0.0040	0.0012	0.97	0.0381(13)
		0	0.6468	0.0041	0.0010	0.38	0.0395(20)
		−0.5	0.6612	0.0040	0.0005	0.20	0.0404(19)
	0.7982	1	0.6394	0.0040		0.77	
		0	0.6555	0.0041		0.41	
		−0.5	0.6663	0.0042		0.23	
F1l	0.6664	1	0.7550	0.0036	0.0010	0.86	0.0446(6)
		0	0.7952	0.0038	0.0012	0.43	0.0466(16)
		−0.5	0.8276	0.0037	0.0001	0.04	0.0476(13)
	0.7323	1	0.7696	0.0045	0.0013	1.33	0.0376(9)
		0	0.8042	0.0048	0.0013	0.49	0.0393(20)
		−0.5	0.8304	0.0048	0.0003	0.12	0.0405(19)
	0.7982	1	0.7829	0.0045		1.29	
		0	0.8125	0.0048		0.59	
		−0.5	0.8328	0.0050		0.26	

the $b = 0$ fit, indicating that the effective fit range for $b = -0.5$ is more on the smaller-r side. We conclude that the range for b from -0.5 to 1 fits well to the data, but with different effective fit ranges. The $b = 0$ fit has the widest effective fit range and will serve as our default choice.

Figure 14 shows the fit results for $\sqrt{8t_0}\Lambda_0$ at the valid flow-time positions for $b = 1, 0, -0.5$ at F1l and F3lLus. We observe that for a fixed choice of b, the values of Λ_0 are constant along the flow-time axis. This indicates that the flow-time dependence of the static force at finite flow time in the distance and flow-time ranges explored in this fixed τ_F analysis is well captured by a constant one-loop gradient flow correction to the static force. We then extrapolate Λ_0 to the zero-flow-time limit with a constant function. The final results of the constant zero-flow-time limits are shown in Table VI.

C. Estimate of the perturbative systematic uncertainties and final results

Up to this point, we have presented results for Λ_0 with error estimates that include only the statistical errors and the systematic errors from choosing different fit ranges. We still need to include the perturbative uncertainty from the unknown higher-order terms in the perturbative expansion. We can do this by varying the scale μ (21). In previous studies of the static energy [14,15,17], the zero-flow-time scale $\mu = 1/r$ was varied by a factor of $\sqrt{2}$. We make here the same choice and vary the parameter s in Eq. (21) from $s = 0.5$ to $s = 2$. We vary the s parameter only in the zero-flow-time part of Eq. (23) and keep it fixed at $s = 1$ in the finite-flow-time part. In principle, we could vary the scale by a factor of 2 instead of $\sqrt{2}$, but it was noted in Ref. [17] that this requires access to quite small distances r. Our current data do not contain small enough distances to allow for this wider variation.

As already stated in the previous sections, the finite-flow-time part of the static force has a considerable dependence on the choice of the parameter b in Eq. (21). To match the conventions of zero-flow-time studies, we choose $b = 0$ as our main result. To estimate the systematic error due to the choice of b and the missing higher-order finite-flow-time perturbative terms, we vary the b parameter between $b = -0.5$ and $b = 1$; for this choice, we refer to the discussion in Appendix A. We vary b only in the finite-flow-time part of Eq. (23).

To arrive at a final result for Λ_0, we have explored several possibilities in Secs. V A, V B 1, and V B 2:

(1) We have performed the constant zero-flow-time limit of the force first, followed by fitting the perturbative expression to the data. This method has the advantage that we do not need to combine the zero-flow-time expression of the force with the one-loop correction coming from the gradient flow. The method does not work, however, at the smallest r, but only for $r/\sqrt{t_0} \geq 0.8$.
(2) We have performed the fit of the combined equation at fixed r along τ_F. This method corresponds to the classical zero-flow-time limit. With this method, the $1/r$ scale has a minor effect, and the method can be applied for only a few r, while the gradient flow scale has a dominant role, which can be seen by the large dependence on the choice of b.
(3) We have performed the fit of the combined equation at fixed τ_F along r. In this method, the $1/r$ scale has a major impact, while the flow timescale has a minor role. This can be seen by the fact that various choices of b fit well to the data.

On the left side of Fig. 15, we compare the results of all three methods at the available perturbative orders. All results agree very well within the errors.

Based on the advantages and disadvantages of all three methods, we chose method 3 with $b = 0$ at F3lLus as the

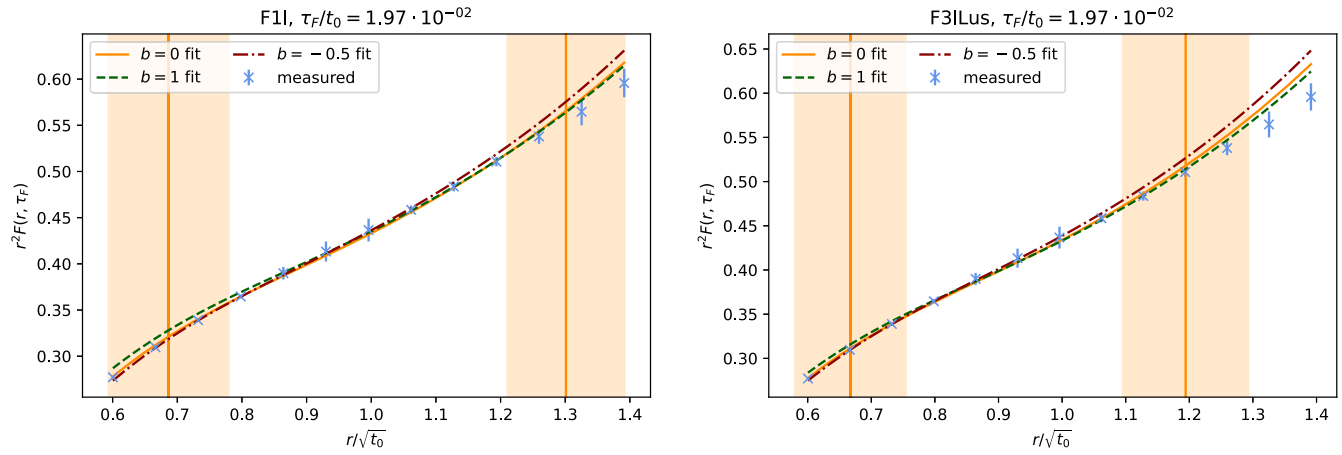

FIG. 13. $\sqrt{8t_0}\Lambda_0$ fit at fixed flow time for different orders. The left vertical line corresponds to the average lower fit limit for $b = 0$, and the right line to its average upper fit limit. The bands around the lines represent the errors of the fit window.

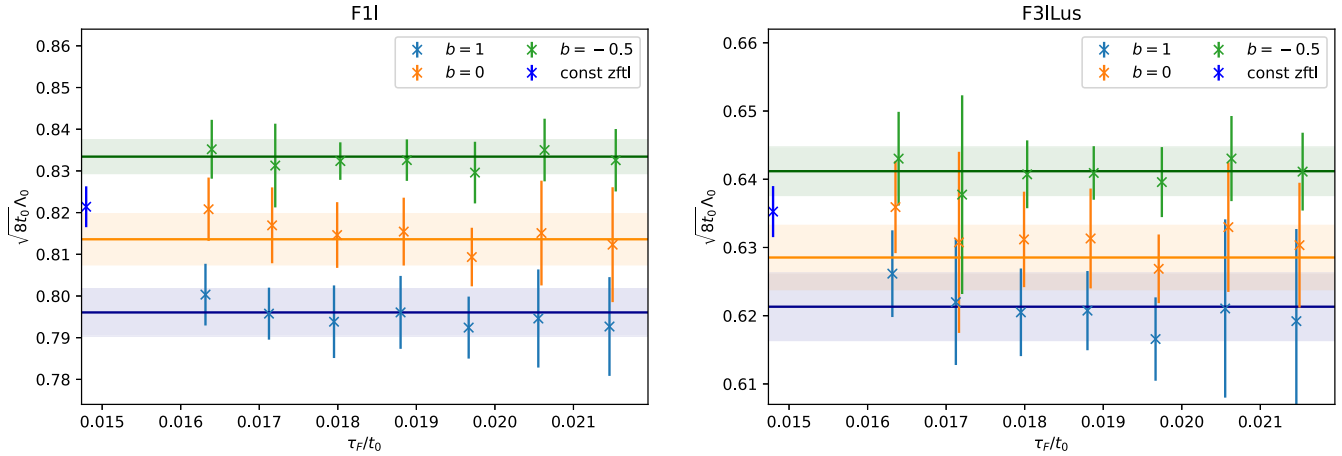

FIG. 14. $\sqrt{8t_0}\Lambda_0$ in the zero-flow-time limit from a constant fit including the statistical and fit errors. We compare different orders and different choices of b. The blue points with the label "const zftl" are the results from Table IV.

main result. Including the uncertainties due to variations of the parameters s and b, we obtain our final result, which reads

$$\sqrt{8t_0}\Lambda_0 = 0.629^{+22}_{-26}, \tag{59}$$

$$\delta(\sqrt{8t_0}\Lambda_0) = (4)^{\text{lattice}}\left(^{+18}_{-25}\right)^{\text{s-scale}}\left(^{+13}_{-7}\right)^{\text{b-scale}}, \tag{60}$$

TABLE VI. Results of the $\sqrt{8t_0}\Lambda_0$ extraction from the constant zero-flow-time limit of Λ_0 at fixed flow time. The error includes the statistical and the AIC error from the fit.

b scale	F1l	F2l	F2lLus	F3l	F3lLus
1	0.7972(56)	0.6591(49)	0.6911(52)	0.6062(52)	0.6218(50)
0	0.8134(57)	0.6649(47)	0.6982(54)	0.6154(44)	0.6287(44)
−0.5	0.8334(42)	0.6709(47)	0.7017(53)	0.6285(35)	0.6415(36)

where $(\ldots)^{\text{lattice}}$ stands for the error coming from the statistics and choosing different fit windows. As we allow the parameters b and s in Eq. (21) to be varied only in the finite- and zero-flow-time parts, respectively, it follows that the systematic uncertainties from these variations are nearly independent one from the other. Hereby, we quote the uncertainty from the b-scale variation measured at $s = 1$ and the uncertainty from the s-scale variation measured at $b = 0$, and we add these in quadrature. This accounts for a conservative estimate of the perturbative error.

On the right side of Fig. 15, we compare our final result with results from previous measurements of Λ_0 [9,63,71–77] and the FLAG average [1]. We only show previous studies that contribute to the FLAG average and a couple of newer studies that have come out since the latest FLAG average. In Fig. 15, the points above the dashed line have been obtained

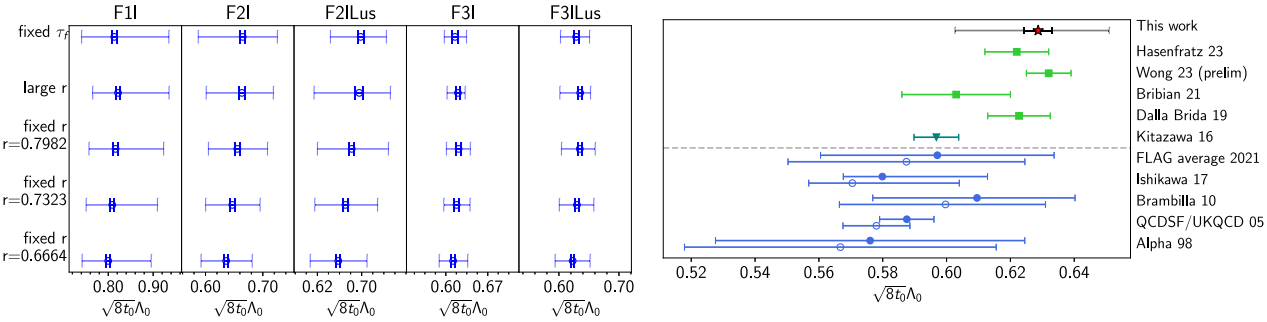

FIG. 15. The final results for $\sqrt{8t_0}\Lambda_0$. Left: Comparison of all fit results for all methods and for all orders. The inner error bar corresponds to the combined statistical and AIC errors, when applicable. The outer error bar represents the total error, including the systematic uncertainties from the scale variation. The row "large r" shows the results from the first method, where we perform the constant zero-flow-time limit of the force first. Right: Our final result compared to the literature. The points above the dashed line were determined with gradient-flow-based scale settings, t_0 (squares) or w_0 (triangle), while the lower points (circles) are converted from r_0 units with either our ratio in Eq. (51) (filled points), or with the ratio from [63] (hollow points).

using the gradient flow-based scales t_0 and w_0,[2] while the points below the dashed line have been obtained from the scale r_0. For the measurements done in the r_0 scale, we convert to the t_0 scale with our own ratio (51) (filled points) or with one of the ratios from Ref. [63] (empty points). We find it remarkable that all the newer studies done in t_0 units are on the higher end of the measurements. Furthermore, we note that our error is larger than other recent studies. Our error is dominated by the perturbative error from the scale variation. Since the scale variation is more prominent at larger distances, it is to be expected that future access to finer lattices could bring this error down. Lastly, with the ratio in Eq. (51), we can convert our final result into r_0 units and obtain

$$r_0\Lambda_0 = 0.657^{+23}_{-28}. \tag{61}$$

VI. SUMMARY AND CONCLUSION

We have shown that the gradient flow renormalizes an operator made of a Wilson loop with a chromoelectric field insertion by reducing discretization effects, and in this way improving the convergence towards the continuum limit. This result can be of use for further studies on operators with different field insertions, which typically show up in nonrelativistic effective field theories.

Thanks to the above property, we are able to perform the continuum limit of the static force at finite flow time, and extrapolate to zero flow time in three different ways. In the first method, we extrapolate the static force from a constant zero-flow-time limit. This works for large and intermediate r, but not at very short distances in the regime $r/\sqrt{t_0} < 0.8$. At large distances, we extract the scales r_0 and r_1, and are able to perform a Cornell fit. For the scales, we find the ratios

$$\frac{r_0}{r_1} = 1.380(14), \tag{62}$$

$$\frac{\sqrt{8t_0}}{r_0} = 0.9569(66), \tag{63}$$

$$\frac{\sqrt{8t_0}}{r_1} = 1.325(13), \tag{64}$$

and for the string tension parameter in the Cornell fit, we find

$$\sigma t_0 = 0.154(6), \tag{65}$$

$$\sigma r_0^2 = 1.345(54), \tag{66}$$

where we have used our result for the ratio $\sqrt{8t_0}/r_0$ in Eq. (63) to convert into r_0 units. At short distances, we fit the perturbative force to the data, and we obtain at F3lLus order

$$\sqrt{8t_0}\Lambda_0 = 0.635(4). \tag{67}$$

In the second and third methods, we fit with a function that combines the force at zero flow time up to three loops with the one-loop flow time correction. In this way, the fit function depends on two scales, r and τ_F. In the second method, we keep r fixed and perform the fit along τ_F. In the third method, we keep τ_F fixed and perform the fit along r, and extrapolate the resulting $\Lambda_0(\tau_F)$ to the zero-flow-time limit. The third method has, in comparison to the second method, a strong dependence on the scale $1/r$, which is the dominant physical scale. Furthermore, the third method reaches out to small r in contrast to the first method.

[2]The measurement of Ref. [74] in w_0 units was transformed to t_0 units using the ratios from [57].

Therefore, we take the third method as our reference method and obtain

$$\sqrt{8t_0}\Lambda_0 = 0.629^{+22}_{-26}, \tag{68}$$

$$\delta(\sqrt{8t_0}\Lambda_0) = (4)^{\text{lattice}}\left(^{+18}_{-25}\right)^{\text{s-scale}}\left(^{+13}_{-7}\right)^{\text{b-scale}}. \tag{69}$$

Using the ratio in Eq. (63), we can give our final result in r_0 units as

$$r_0\Lambda_0 = 0.657^{+23}_{-28}. \tag{70}$$

Nevertheless, all methods agree well within their errors, with an overlap of almost 70%.

ACKNOWLEDGMENTS

We would like to thank Johannes H. Weber for useful discussions. The lattice QCD calculations were performed using the publicly available MILC code. The simulations were carried out on the computing facilities of the Computational Center for Particle and Astrophysics (C2PAP), the Leibniz-Rechenzentrum (LRZ) in the project "Calculation of finite-T QCD correlators" (pr83pu), and the SuperMUC cluster at the LRZ in the project "The role of the charm-quark for the QCD coupling constant" (pn56bo). J. M.-S. acknowledges support by the Munich Data Science Institute (MDSI) at the Technical University of Munich (TUM) via the Linde/MDSI Doctoral Fellowship program. This research was funded by the Deutsche Forschungsgemeinschaft (DFG, German Research Foundation) cluster of excellence "ORIGINS" (www.origins-cluster.de) under Germany's Excellence Strategy No. EXC-2094-390783311. The work of N. B. and J. M.-S. is supported by the DFG (Deutsche Forschungsgemeinschaft, German Research Foundation) under Grant No. BR 4058/2-2. N. B., J. M.-S., and A. V. acknowledge support from the STRONG-2020 European Union's Horizon 2020 research and innovation program under Grant Agreement No. 824093.

APPENDIX A: ABOUT NEGATIVE VALUES OF b IN μ

In the analysis done in Sec. V, we chose the scale (21) with different values for b, including negative values. The ratio $\mathcal{F}^L_{\text{NLO}}(r,\tau_F,\mu)/\mathcal{F}_0(r,\tau_F)$ for different values of the parameters s and b is shown in Fig. 16. In [37], the choices $b=1$, 0 with $s=1$, and $b=1$ with $s=0$ were also analyzed. The choice $s=1$, $b=0$ is the natural choice at zero flow time, since for it, the $\log(\mu r)$ terms vanish. However, this choice does not capture $\log(\mu\sqrt{\tau_F})$ terms that become important at large flow time. This is shown by the ratio $\mathcal{F}^L_{\text{NLO}}(r,\tau_F,\mu)/\mathcal{F}_0(r,\tau_F)$ becoming large at large flow times for this choice of parameters. The choice $s=0$, $b=1$ is the natural choice at large flow time, since for it, the $\log(\mu\sqrt{\tau_F})$ terms vanish. However, this choice does not capture $\log(\mu r)$ terms that become important at small flow times. This is shown by the ratio $\mathcal{F}^L_{\text{NLO}}(r,\tau_F,\mu)/\mathcal{F}_0(r,\tau_F)$ becoming large at small flow times for this choice of parameters. The choice of $s=1$ and $b=1$ interpolates between these two extreme and provides a small $\mathcal{F}^L_{\text{NLO}}(r,\tau_F,\mu)$ correction with respect to the leading gradient flow term $\mathcal{F}_0(r,\tau_F)$ over the whole range of flow times. Also, the overall scale dependence turns out to be weak with this scale choice.

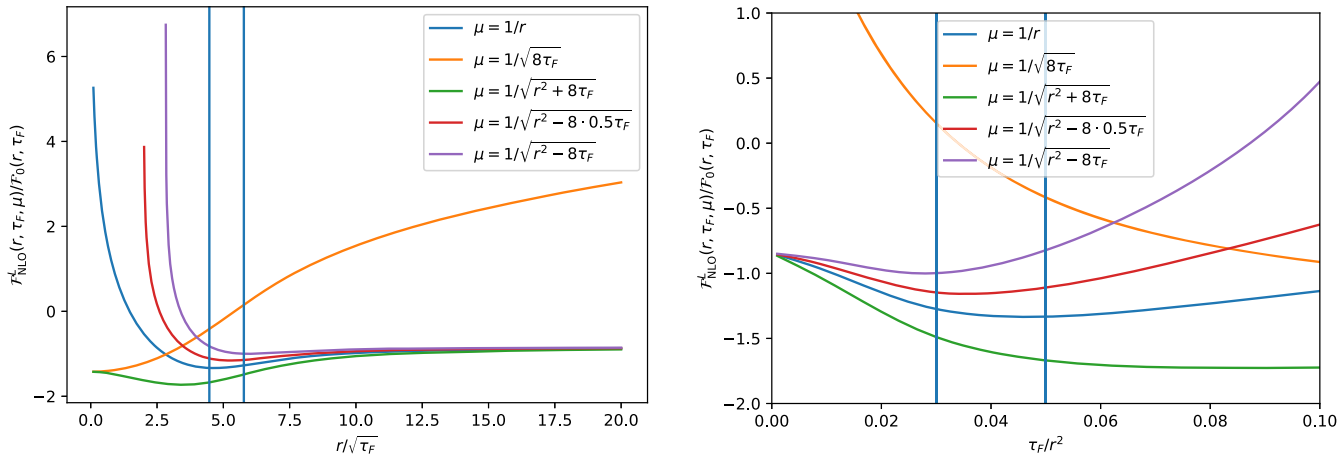

FIG. 16. Left: The ratio $\mathcal{F}^L_{\text{NLO}}(r,\tau_F,\mu)/\mathcal{F}_0(r,\tau_F)$ [see Eq. (15)] as a function of $r/\sqrt{\tau_F}$ plotted for various values of s and b. The vertical lines represent the characteristic flow-time window of this study. The left limit on the x axis corresponds to the infinite-flow-time limit, while the right limit corresponds to the zero-flow-time limit. Right: The same ratio, but as a function of τ_F/r^2 zoomed around the region of interest.

Nevertheless, our lattice data explore a very specific and limited region of flow-time values, the region in between the vertical lines in Fig. 16. A zoomed-in view of this region is shown in the right plot that makes manifest that different choices of b, keeping $s = 1$, provide, indeed, even smaller and more stable corrections $\mathcal{F}^L_{\mathrm{NLO}}(r, \tau_F, \mu)$ in the region of interest than the choice $b = 1$. In particular, this is the case for $b = 0$ and $b = -0.5$, which indeed best fit our lattice data, as we have discussed in the main body of the paper. More negative values of b further reduce the relative size of $\mathcal{F}^L_{\mathrm{NLO}}(r, \tau_F, \mu)$, but they make it more scale dependent. Hence, the one-loop expression of the gradient flow expression of the force suggests that for $0.03 \lesssim \tau_F/r^2 \lesssim 0.05$, the ideal choice of the parameter b is in between 0 and a negative number larger than -1. This is confirmed by the lattice data. Clearly, also, a parametrization with negative b must smoothly go over $\mu = 1/\sqrt{\tau_F}$ at large flow time. However, the specific form of the parametrization at large flow times, $\tau_F/r^2 > 0.05$, cannot be explored with the present data.

APPENDIX B: FLOW-TIME DEPENDENCE OF THE WILSON LOOPS WITH AND WITHOUT CHROMOELECTRIC FIELD INSERTIONS

The Wilson loops with and without chromoelectric field insertion are the main objects of this work; therefore, it is worth to have a closer look on the flow-time dependence of them. Figure 17 shows the T dependence of the Wilson loops at different flow times. In a logarithmic y scale, we see linear, decreasing curves for large T, which correspond to the exponential falloff controlled by the static energy. For zero and small flow times, the slope is the same; for larger flow times, the slope becomes more flat. This reflects the flow-time dependency of the static energy. This observation holds for Wilson loops with and without chromoelectric field insertions.

Figure 18 shows the flow-time dependence of the Wilson loops with and without chromoelectric field insertion at fixed r and T. We see a strong flow-time dependence for both cases caused by the divergence of the static quark propagator. The strong flow-time dependence cancels in the ratio of the Wilson loops.

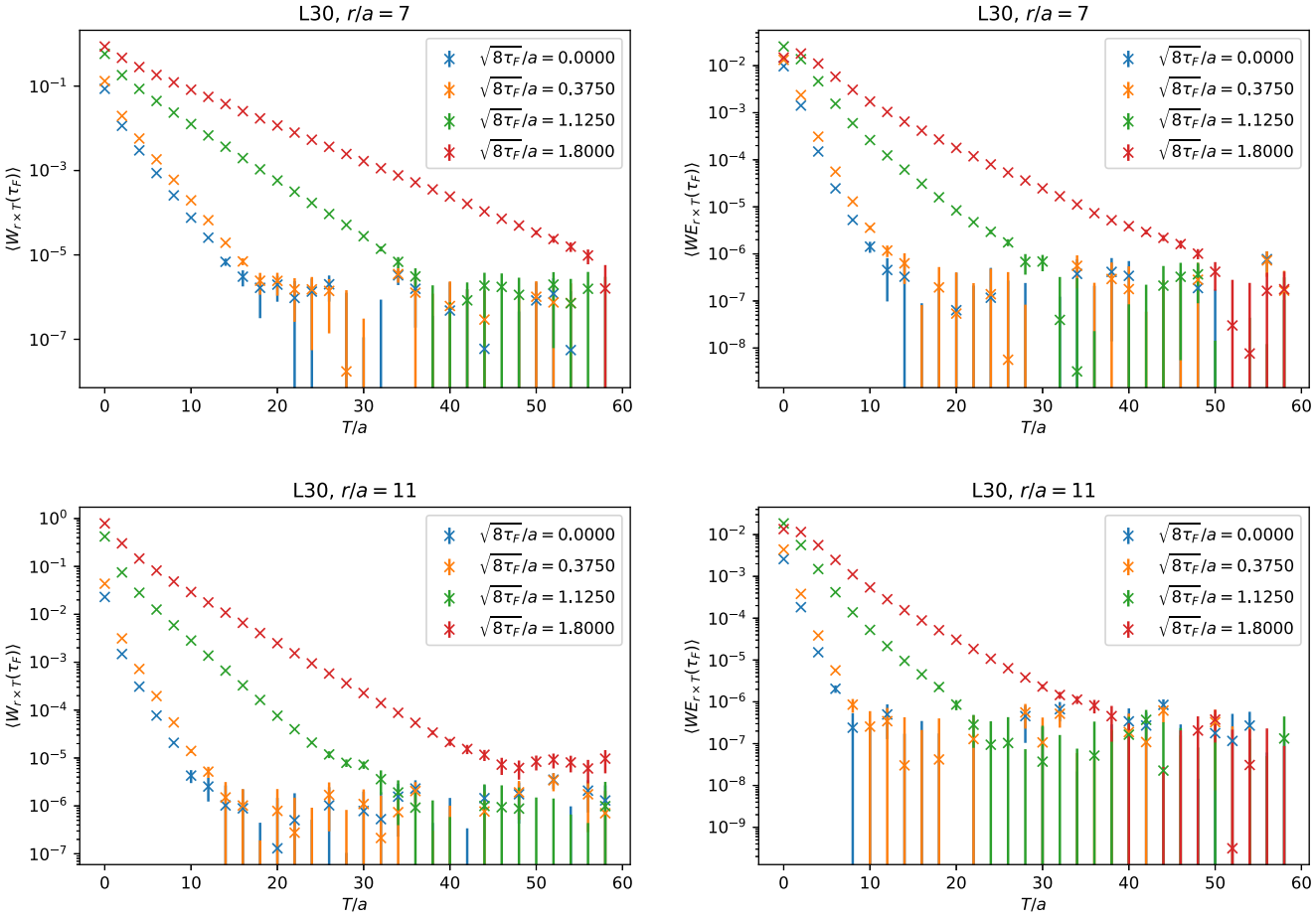

FIG. 17. The left sides show the T dependence of the Wilson loops at four different fixed flow times and for two fixed r. The right sides show the same for the Wilson loops with a chromoelectric field insertion.

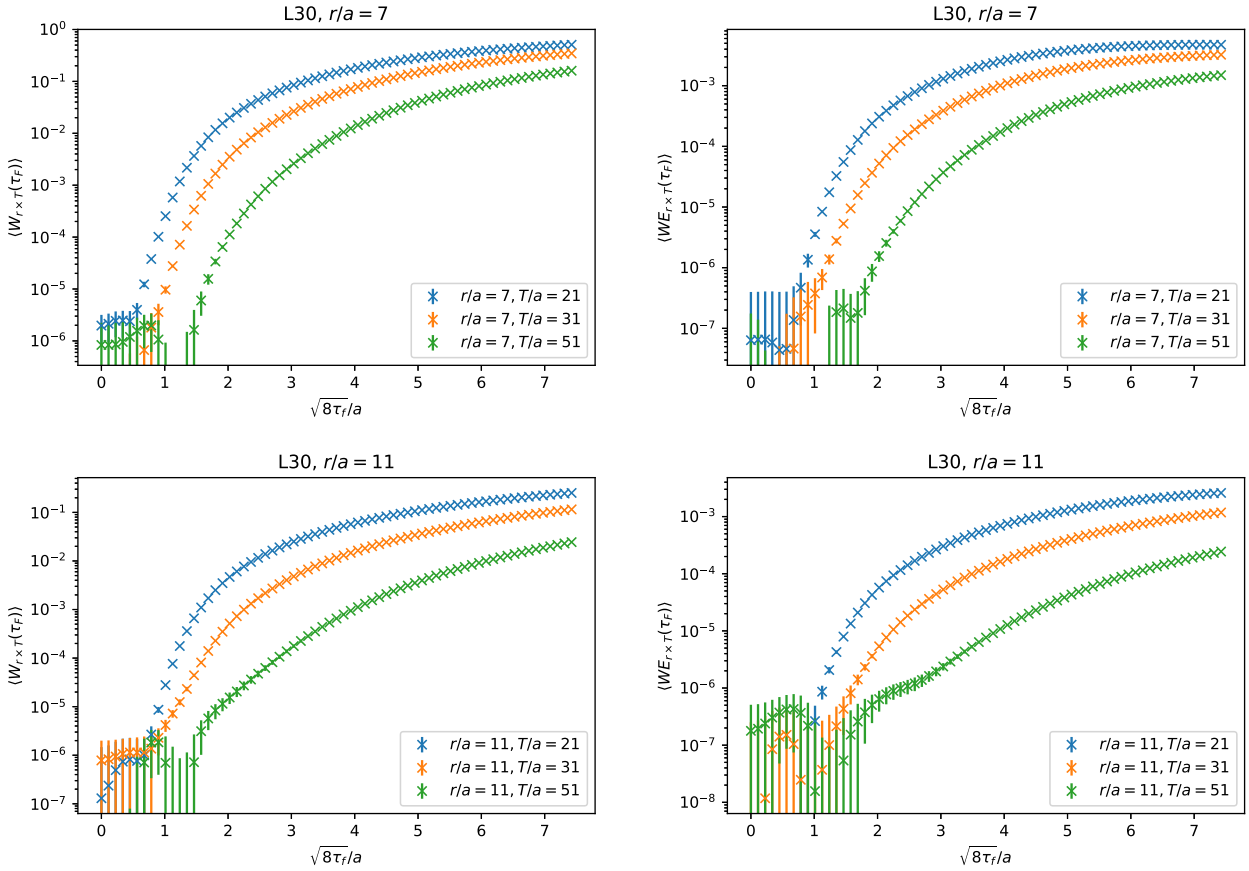

FIG. 18. The left sides show the flow-time dependence of the Wilson loop at several fixed T and at two different r values. The right sides show the same for the Wilson loops with a chromoelectric field insertion.

APPENDIX C: AUTOCORRELATION TIMES ON L40

To reduce the integrated autocorrelation times, we block the data to 30 jackknife blocks per ensemble. Apart from our largest lattice (L40), this choice leads to 200 configs per block, which is considerably higher than the integrated autocorrelation times $\tau_{\mathrm{int}} \lesssim \mathcal{O}(10)$ for all the relevant observables including the topological charge Q. However, we have less statistics for the L40 lattice, which leads to only 110 configurations per block. Moreover, we observe slower fluctuation of topological charge for the L40 lattice with $\tau_{\mathrm{int}} = 101.6$ for the unblocked data. To see whether the block size is large enough also for this ensemble, we plot $\tau_{\mathrm{int}}(Q^2)$ as a function of the block size[3] in Fig. 19. We observe that even the topological charge has a τ_{int} of order 1, at our chosen block size. More importantly, we also note that the static force has autocorrelation times below 1 for all possible block sizes. This is expected, as the static energy is known to be moderately unaffected by the topological slowing down [49]. Similar topology independence has also been observed for other methods of determining the strong coupling constant [78].

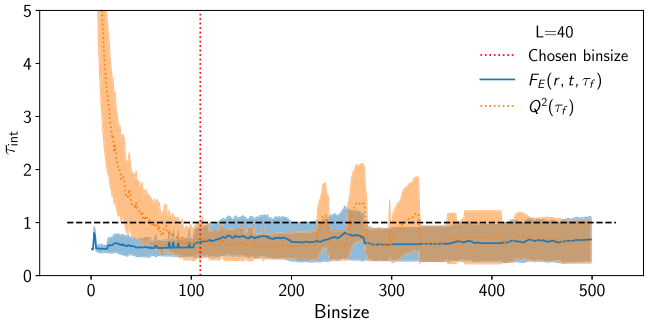

FIG. 19. Integrated autocorrelation time τ_{int} as a function of the block size for the largest lattice ensemble L40. The curve with a solid line shows the autocorrelation time for the static force, while the dashed curve shows τ_{int} for the topological charge squared, and the vertical line indicates our chosen blocking.

[3]We note that for the topological charge squared Q^2, which is related to the topological susceptibility, the integrated autocorrelation times for the unblocked data are about half of the τ_{int} for the Q.

[1] Y. Aoki *et al.* (Flavour Lattice Averaging Group (FLAG) Collaboration), FLAG review 2021, Eur. Phys. J. C **82**, 869 (2022).

[2] D. d'Enterria *et al.*, The strong coupling constant: State of the art and the decade ahead, arXiv:2203.08271.

[3] Mattia Dalla Brida, Roman Höllwieser, Francesco Knechtli, Tomasz Korzec, Alessandro Nada, Alberto Ramos, Stefan Sint, and Rainer Sommer (ALPHA Collaboration), Determination of $\alpha_s(m_Z)$ by the non-perturbative decoupling method, Eur. Phys. J. C **82**, 1092 (2022).

[4] Silvia Necco and Rainer Sommer, The $N(f) = 0$ heavy quark potential from short to intermediate distances, Nucl. Phys. **B622**, 328 (2002).

[5] Marco Guagnelli, Rainer Sommer, and Hartmut Wittig (ALPHA Collaboration), Precision computation of a low-energy reference scale in quenched lattice QCD, Nucl. Phys. **B535**, 389 (1998).

[6] R. Sommer, A new way to set the energy scale in lattice gauge theories and its applications to the static force and α_s in SU(2) Yang-Mills theory, Nucl. Phys. **B411**, 839 (1994).

[7] Gunnar S. Bali and Klaus Schilling, Running coupling and the Lambda parameter from SU(3) lattice simulations, Phys. Rev. D **47**, 661 (1993).

[8] S. P. Booth, D. S. Henty, A. Hulsebos, A. C. Irving, Christopher Michael, and P. W. Stephenson (UKQCD Collaboration), The running coupling from SU(3) lattice gauge theory, Phys. Lett. B **294**, 385 (1992).

[9] Nora Brambilla, Xavier Garcia i Tormo, Joan Soto, and Antonio Vairo, Precision determination of $r_0\Lambda_{\overline{\rm MS}}$ from the QCD static energy, Phys. Rev. Lett. **105**, 212001 (2010); **108**, 269903(E) (2012).

[10] Nikolai Husung, Mateusz Koren, Philipp Krah, and Rainer Sommer, SU(3) Yang Mills theory at small distances and fine lattices, EPJ Web Conf. **175**, 14024 (2018).

[11] Nikolai Husung, Peter Marquard, and Rainer Sommer, Asymptotic behavior of cutoff effects in Yang-Mills theory and in Wilson's lattice QCD, Eur. Phys. J. C **80**, 200 (2020).

[12] Karl Jansen, Felix Karbstein, Attila Nagy, and Marc Wagner (ETM Collaboration), $\Lambda_{\overline{\rm MS}}$ from the static potential for QCD with $n_f = 2$ dynamical quark flavors, J. High Energy Phys. 01 (2012) 025.

[13] Felix Karbstein, Antje Peters, and Marc Wagner, $\Lambda_{\overline{\rm MS}}^{(n_f=2)}$ from a momentum space analysis of the quark-antiquark static potential, J. High Energy Phys. 09 (2014) 114.

[14] Alexei Bazavov, Nora Brambilla, Xavier Garcia i Tormo, Peter Petreczky, Joan Soto, and Antonio Vairo, Determination of α_s from the QCD static energy, Phys. Rev. D **86**, 114031 (2012).

[15] Alexei Bazavov, Nora Brambilla, Xavier Garcia i Tormo, Peter Petreczky, Joan Soto, and Antonio Vairo, Determination of α_s from the QCD static energy: An update, Phys. Rev. D **90**, 074038 (2014); **101**, 119902(E) (2020).

[16] Hiromasa Takaura, Takashi Kaneko, Yuichiro Kiyo, and Yukinari Sumino, Determination of α_s from static QCD potential: OPE with renormalon subtraction and lattice QCD, J. High Energy Phys. 04 (2019) 155.

[17] Alexei Bazavov, Nora Brambilla, Xavier Garcia i Tormo, Péter Petreczky, Joan Soto, Antonio Vairo, and Johannes Heinrich Weber (TUMQCD Collaboration), Determination of the QCD coupling from the static energy and the free energy, Phys. Rev. D **100**, 114511 (2019).

[18] Cesar Ayala, Xabier Lobregat, and Antonio Pineda, Determination of $\alpha(M_z)$ from an hyperasymptotic approximation to the energy of a static quark-antiquark pair, J. High Energy Phys. 09 (2020) 016.

[19] Nora Brambilla, Antonio Pineda, Joan Soto, and Antonio Vairo, The infrared behavior of the static potential in perturbative QCD, Phys. Rev. D **60**, 091502 (1999).

[20] Antonio Pineda and Joan Soto, The renormalization group improvement of the QCD static potentials, Phys. Lett. B **495**, 323 (2000).

[21] Nora Brambilla, Xavier Garcia i Tormo, Joan Soto, and Antonio Vairo, The logarithmic contribution to the QCD static energy at N^{4}LO, Phys. Lett. B **647**, 185 (2007).

[22] Nora Brambilla, Antonio Vairo, Xavier Garcia i Tormo, and Joan Soto, The QCD static energy at NNNLL, Phys. Rev. D **80**, 034016 (2009).

[23] C. Anzai, Y. Kiyo, and Y. Sumino, Static QCD potential at three-loop order, Phys. Rev. Lett. **104**, 112003 (2010).

[24] Alexander V. Smirnov, Vladimir A. Smirnov, and Matthias Steinhauser, Three-loop static potential, Phys. Rev. Lett. **104**, 112002 (2010).

[25] Antonio Vairo, A low-energy determination of α_s at three loops, EPJ Web Conf. **126**, 02031 (2016).

[26] Antonio Vairo, Strong coupling from the QCD static energy, Mod. Phys. Lett. A **31**, 1630039 (2016).

[27] Nora Brambilla, Antonio Pineda, Joan Soto, and Antonio Vairo, The QCD potential at $O(1/m)$, Phys. Rev. D **63**, 014023 (2001).

[28] Nora Brambilla, Viljami Leino, Owe Philipsen, Christian Reisinger, Antonio Vairo, and Marc Wagner, Lattice gauge theory computation of the static force, Phys. Rev. D **105**, 054514 (2022).

[29] R. Narayanan and H. Neuberger, Infinite N phase transitions in continuum Wilson loop operators, J. High Energy Phys. 03 (2006) 064.

[30] Martin Lüscher, Trivializing maps, the Wilson flow and the HMC algorithm, Commun. Math. Phys. **293**, 899 (2010).

[31] Martin Lüscher, Properties and uses of the Wilson flow in lattice QCD, J. High Energy Phys. 08 (2010) 071; 03 (2014) 92.

[32] Andreas Risch, Stefan Schaefer, and Rainer Sommer, The influence of gauge field smearing on discretisation effects, Proc. Sci., LATTICE2022 (**2023**) 384.

[33] Andreas Risch, Gauge field smearing and controlled continuum extrapolations, in 40th International Symposium on Lattice Field Theory, Proc. Sci., LATTICE2023 (**2024**) 342.

[34] Masanori Okawa and Antonio Gonzalez-Arroyo, String tension from smearing and Wilson flow methods, Proc. Sci., LATTICE2014 (**2014**) 327.

[35] Alexei Bazavov, Daniel Hoying, Olaf Kaczmarek, Rasmus N. Larsen, Swagato Mukherjee, Peter Petreczky, Alexander Rothkopf, and Johannes Heinrich Weber, Unscreened forces in quark-gluon plasma?, Phys. Rev. D **109**, 074504 (2024).

[36] Alexei Bazavov and Thomas Chuna, Efficient integration of gradient flow in lattice gauge theory and properties of low-storage commutator-free Lie group methods, arXiv:2101.05320.

[37] Nora Brambilla, Hee Sok Chung, Antonio Vairo, and Xiang-Peng Wang, QCD static force in gradient flow, J. High Energy Phys. 01 (2022) 184.
[38] Viljami Leino, Nora Brambilla, Julian Mayer-Steudte, and Antonio Vairo, The static force from generalized Wilson loops using gradient flow, EPJ Web Conf. **258**, 04009 (2022).
[39] Julian Mayer-Steudte, Nora Brambilla, Viljami Leino, and Antonio Vairo, Implications of gradient flow on the static force, Proc. Sci., LATTICE2022 (**2023**) 353.
[40] Kenneth G. Wilson, Confinement of quarks, Phys. Rev. D **10**, 2445 (1974).
[41] Martin Luscher, Topology, the Wilson flow and the HMC algorithm, Proc. Sci., LATTICE2010 (**2010**) 015.
[42] Martin Luscher and Peter Weisz, Perturbative analysis of the gradient flow in non-Abelian gauge theories, J. High Energy Phys. 02 (2011) 051.
[43] Patrick Fritzsch and Alberto Ramos, The gradient flow coupling in the Schrödinger functional, J. High Energy Phys. 10 (2013) 008.
[44] Sundance O. Bilson-Thompson, Derek B. Leinweber, and Anthony G. Williams, Highly improved lattice field strength tensor, Ann. Phys. (Amsterdam) **304**, 1 (2003).
[45] G. Peter Lepage and Paul B. Mackenzie, On the viability of lattice perturbation theory, Phys. Rev. D **48**, 2250 (1993).
[46] C. Christensen and M. Laine, Perturbative renormalization of the electric field correlator, Phys. Lett. B **755**, 316 (2016).
[47] Nora Brambilla, Viljami Leino, Julian Mayer-Steudte, and Peter Petreczky (TUMQCD Collaboration), Heavy quark diffusion coefficient with gradient flow, Phys. Rev. D **107**, 054508 (2023).
[48] Luis Altenkort, Alexander M. Eller, Olaf Kaczmarek, Lukas Mazur, Guy D. Moore, and Hai-Tao Shu, Heavy quark momentum diffusion from the lattice using gradient flow, Phys. Rev. D **103**, 014511 (2021).
[49] Johannes Heinrich Weber, Alexei Bazavov, and Peter Petreczky, Equation of state in $(2+1)$ flavor QCD at high temperatures, Proc. Sci., Confinement2018 (**2019**) 166.
[50] Patrick Fritzsch, Alberto Ramos, and Felix Stollenwerk, Critical slowing down and the gradient flow coupling in the Schrödinger functional, Proc. Sci., Lattice2013 (**2014**) 461.
[51] Carolin Schlosser and Marc Wagner, Hybrid static potentials in SU(3) lattice gauge theory at small quark-antiquark separations, Phys. Rev. D **105**, 054503 (2022).
[52] William I. Jay and Ethan T. Neil, Bayesian model averaging for analysis of lattice field theory results, Phys. Rev. D **103**, 114502 (2021).
[53] Zoltan Fodor, Kieran Holland, Julius Kuti, Santanu Mondal, Daniel Nogradi, and Chik Him Wong, The lattice gradient flow at tree-level and its improvement, J. High Energy Phys. 09 (2014) 018.
[54] Claude W. Bernard, Tom Burch, Kostas Orginos, Doug Toussaint, Thomas A. DeGrand, Carleton E. DeTar, Steven A. Gottlieb, Urs M. Heller, James E. Hetrick, and Bob Sugar, The static quark potential in three flavor QCD, Phys. Rev. D **62**, 034503 (2000).
[55] Rainer Sommer, Scale setting in lattice QCD, Proc. Sci., LATTICE2013 (**2014**) 015.
[56] Mattia Bruno and Rainer Sommer (ALPHA Collaboration), On the N_f-dependence of gluonic observables, Proc. Sci., LATTICE2013 (**2014**) 321.
[57] Masayuki Asakawa, Tetsuo Hatsuda, Takumi Iritani, Etsuko Itou, Masakiyo Kitazawa, and Hiroshi Suzuki, Determination of reference scales for wilson gauge action from Yang-Mills gradient flow, arXiv:1503.06516.
[58] A. Francis, O. Kaczmarek, M. Laine, T. Neuhaus, and H. Ohno, Critical point and scale setting in SU(3) plasma: An update, Phys. Rev. D **91**, 096002 (2015).
[59] Marco Cè, Cristian Consonni, Georg P. Engel, and Leonardo Giusti, Non-Gaussianities in the topological charge distribution of the SU(3) Yang-Mills theory, Phys. Rev. D **92**, 074502 (2015).
[60] Norihiko Kamata and Shoichi Sasaki, Numerical study of tree-level improved lattice gradient flows in pure Yang-Mills theory, Phys. Rev. D **95**, 054501 (2017).
[61] Francesco Knechtli, Tomasz Korzec, Björn Leder, and Graham Moir (ALPHA Collaboration), Power corrections from decoupling of the charm quark, Phys. Lett. B **774**, 649 (2017).
[62] Leonardo Giusti and Martin Lüscher, Topological susceptibility at $T > T_c$ from master-field simulations of the SU(3) gauge theory, Eur. Phys. J. C **79**, 207 (2019).
[63] Mattia Dalla Brida and Alberto Ramos, The gradient flow coupling at high-energy and the scale of SU(3) Yang-Mills theory, Eur. Phys. J. C **79**, 720 (2019).
[64] Yoshiaki Koma, Miho Koma, and Hartmut Wittig, Relativistic corrections to the static potential at $O(1/m)$ and $O(1/m^2)$, *Proc. Sci.*, LATTICE2007 (2007) 111 [arXiv:0711.2322].
[65] Antonio Gonzalez-Arroyo and Masanori Okawa, The string tension from smeared Wilson loops at large N, Phys. Lett. B **718**, 1524 (2013).
[66] Biagio Lucini, Michael Teper, and Urs Wenger, The high temperature phase transition in SU(N) gauge theories, J. High Energy Phys. 01 (2004) 061.
[67] B. Beinlich, F. Karsch, E. Laermann, and A. Peikert, String tension and thermodynamics with tree level and tadpole improved actions, Eur. Phys. J. C **6**, 133 (1999).
[68] K. G. Chetyrkin, Johann H. Kuhn, and M. Steinhauser, RunDec: A Mathematica package for running and decoupling of the strong coupling and quark masses, Comput. Phys. Commun. **133**, 43 (2000).
[69] Barbara Schmidt and Matthias Steinhauser, CRunDec: A C++ package for running and decoupling of the strong coupling and quark masses, Comput. Phys. Commun. **183**, 1845 (2012).
[70] Florian Herren and Matthias Steinhauser, Version 3 of RunDec and CRunDec, Comput. Phys. Commun. **224**, 333 (2018).
[71] Stefano Capitani, Martin Lüscher, Rainer Sommer, and Hartmut Wittig, Non-perturbative quark mass renormalization in quenched lattice QCD, Nucl. Phys. **B544**, 669 (1999); **B582**, 762(E) (2000).
[72] M. Gockeler, R. Horsley, A. C. Irving, D. Pleiter, P. E. L. Rakow, G. Schierholz, and H. Stuben, A determination of the Lambda parameter from full lattice QCD, Phys. Rev. D **73**, 014513 (2006).

[73] Ken-Ichi Ishikawa, Issaku Kanamori, Yuko Murakami, Ayaka Nakamura, Masanori Okawa, and Ryoichiro Ueno, Non-perturbative determination of the Λ-parameter in the pure SU(3) gauge theory from the twisted gradient flow coupling, J. High Energy Phys. 12 (2017) 067.

[74] Masakiyo Kitazawa, Takumi Iritani, Masayuki Asakawa, Tetsuo Hatsuda, and Hiroshi Suzuki, Equation of state for SU(3) gauge theory via the energy-momentum tensor under gradient flow, Phys. Rev. D **94**, 114512 (2016).

[75] Eduardo I. Bribian, Jorge Luis Dasilva Golan, Margarita Garcia Perez, and Alberto Ramos, Memory efficient finite volume schemes with twisted boundary conditions, Eur. Phys. J. C **81**, 951 (2021).

[76] Chik Him Wong, Szabolcs Borsanyi, Zoltan Fodor, Kieran Holland, and Julius Kuti, Toward a novel determination of the strong QCD coupling at the Z-pole, Proc. Sci., LATTICE2022 (**2023**) 043.

[77] Anna Hasenfratz, Curtis Taylor Peterson, Jake van Sickle, and Oliver Witzel, Λ parameter of the SU(3) Yang-Mills theory from the continuous β function, Phys. Rev. D **108**, 014502 (2023).

[78] Claudio Bonanno, Jorge Luis Dasilva Golán, Massimo D'Elia, Margarita García Pérez, and Andrea Giorgieri, The SU(3) twisted gradient flow strong coupling without topology freezing, arXiv:2403.13607.